

THORIUM-BASED MIRRORS IN THE EXTREME ULTRAVIOLET

by

Nicole Farnsworth

Submitted to the Department of Physics and Astronomy in partial fulfillment
of the requirements for the degree of

Bachelor of Science

Brigham Young University

April 2005

R. Steven Turley, Advisor

Eric N. Jellen, Thesis Coordinator

Scott D. Sommerfeldt, Department Chair

Copyright © 2005 Nicole Farnsworth

All Rights Reserved

ABSTRACT

THORIUM-BASED MIRRORS IN THE EXTREME ULTRAVIOLET

Nicole Farnsworth

Department of Physics and Astronomy

Bachelor of Science

As applications for optics in the EUV (100 – 1000 Angstroms) have increased, the demand for better reflectors in this region has also increased. Here, thorium and thorium oxide films were deposited using RF-sputtering and characterized with atomic force microscopy (AFM), x-ray diffraction (XRD), and x-ray photoelectron spectroscopy (XPS). We have measured the reflection and transmission of these films at the Advanced Light Source in order to determine the optical constants of thorium and thorium oxide. Thorium films were found to be characteristically rough with an RMS roughness of 3.6 *nm* over a 100×100 *nm* area and an RMS roughness of 4.3 *nm* over a 1000×1000 *nm* area. We have also found that thorium tends to oxidize on the surface. In our sample we found nearly linear oxidation for 50 Å. We have attempted to account for this roughness and oxidation using three methods, the Debye-Waller and Nevot-Croce scalar correction factors and the finite differences approximation. We conclude that the best way to account for roughness and surface oxidation in our program is to employ a combination of the Nevot-Croce factor and the finite

differences approximation. We have found that the best way to avoid problems with oxidation is to use thorium oxide films. We have found values for δ for thorium oxide in the region from $115 - 250 \text{ \AA}$. We have found that we cannot find β values that we believe because reflectance and transmittance measurements give us two different and irreconcilable sets of data. We are unsure at this point why the two measurements give us different answers.

ACKNOWLEDGMENTS

I would like to thank my advisor, Dr. Steve Turley for the countless hours he has spent with me on this project. I would also like to thank Dr. David Allred for his assistance and care. I am grateful to all of the BYU Thin Films Research Group for their valuable assistance on this project. This project was funded in part by the BYU Physics Department and by the National Science Foundation. I would also like to thank my parents and my sisters for their love and support through my undergraduate experience.

Contents

1	Introduction	1
1.1	Interest in the Extreme Ultraviolet and Thorium based mirrors	1
1.2	Project Background	2
1.3	Theory	3
1.3.1	Optical Constants	3
1.3.2	Experimentally determining optical constants	7
1.3.3	Roughness	13
1.3.4	Accepted methods of accounting for roughness	14
1.3.5	Project Focus	17
1.3.6	Film Deposition	17
1.3.7	Characterization theory	18
2	Roughness	20
2.1	Characterization of Roughness	22
2.2	Problems with Characterization	23
2.3	Accounting for Roughness	30
3	Finding the Optical Constants of Thorium Oxide	33
3.1	Reflectance and Transmittance Measurements	33

<i>CONTENTS</i>	vii
3.2 Reflectance and Transmittance Data	40
3.3 Data Fitting	44
4 Conclusions	57

List of Tables

3.1 Grating, filter, and order sorters used to achieve spectral purity for the given wavelength range.	35
---	----

List of Figures

1.1	CXRO computed reflectance as a function of wavelength at 15° . Although gold and nickel are two commonly used reflector materials in this region, thorium based mirrors may be more reflective at wavelengths longer than 160 \AA	3
1.2	The geometry used to calculate theoretical reflectance and transmittance.	6
1.3	a) a monochromator b) reflection measurement c) transmission measurement	8
1.4	Large scale roughness results in diffuse scattering, decreasing the reflectivity of the surface at the specular angle.	14
1.5	Interdiffusion of layers. In an ideal multilayer, composition changes infinitely fast from one material to another. In real multilayers, interfaces have a finite width. left: an infinitely sharp boundary right: a diffuse boundary	15
1.6	Surface roughness in a film can be approximated as a series of steps in density from vacuum to the material.	16
1.7	A schematic of the finite differences approximation. A gradient in the index of refraction between points a and b is approximated as a finite number of layers whose indices of refraction vary linearly from n_1 to n_2 .	17

1.8 The photoelectric effect 18

1.9 AFM tip 19

2.1 Reflectance data for a single layer of thorium on a Silicon substrate at 150 Å. Along the x-axis is plotted angle, and along the y-axis is plotted reflectance. The fit assumes smooth boundaries and abrupt interfaces. The inset shows the poorness of the fit at middle angles (10-30 degrees). 21

2.2 Atomic force microscopy profiles of thorium at two length scales: 100x100nm and 1000x1000nm. At the 100x100nm length scale, RMS roughness equals 3.6nm. At the 1000x1000nm length scale, RMS roughness equals 4.3nm. 22

2.3 Power spectral density plot of thorium. The highest density of roughness occurs in the range from 40 to 80 nm, small-scale roughness. . . 23

2.4 X-ray photoelectron spectroscopy depth profile of Thorium. The surface of the sample has oxidized nearly linearly for about 50 Å. The Thorium-Silicon edge gives as an idea of the resolution of this technique because we assume that this boundary is sharp. 24

2.5 An AFM tip that is on the order of the size of the roughness being measured cannot characterize roughness accurately. 24

2.6 A rough surface approximated by Gaussian random numbers (red line). The blue line is the surface as measured by the AFM tip. The RMS roughness of the surface is 1.03 nm while the RMS roughness detected by the tip was 0.23 nm. 25

2.7	The power spectral density of the surface (red) and the surface detected by the tip (blue). For this surface, the tip not only fails to detect high frequency roughness on the surface, it actually detects more low frequency roughness than is actually present.	26
2.8	A rough surface approximated by correlated Gaussian random numbers (red line). The blue line is the surface as measured by the AFM tip. The RMS roughness of the surface is 1.49 nm while the RMS roughness detected by the tip was 1.33 nm.	27
2.9	The power spectral density of the surface (red) and the surface detected by the tip (blue). For this surface, the PSD of the real surface and the surface detected by the tip match almost identically.	28
2.10	The power spectral density of the surface (red) and the surface detected by the tip blue. As the length scale of correlation gets longer, the PSD measured by the tip gets closer to the actual PSD of the surface.	29
2.11	Fit of thorium reflection data after correction using the Debye-Waller factor. The factor improved the fit only at low angles.	30
2.12	Fit of thorium reflection data after correction using the Nevot-Croce factor. The factor improved the fit significantly at low and high angles.	31
2.13	Fit of thorium reflection data with a 50 Angstrom transition layer approximated as five 10 Angstrom layers whose indices of refraction varied linearly. The approximation improved the fit significantly at low and middle angles.	32
3.1	A schematic layout of ALS beamline 6.3.2.	34
3.2	Beam intensity at the sample position.	35
3.3	Monochromator resolution.	36

3.4	Reflectance of ThO ₂ on Si measured with two filter sets at 14 ⁰ . The two measurements disagree by as much as 0.013.	37
3.5	A second grating was placed at the sample stage and rotated with respect to a fixed detector. The two data sets were taken with two different filter sets with a wavelength of 180 Å. The inset shows spectral impurities in the wavelength produced by the silicon filter set.	38
3.6	Sample stage axis specifications for beamline 6.3.2 reflectometer.	38
3.7	A typical dark current scan taken as a function of wavelength.	39
3.8	Reflection of ThO ₂ on polyimide film at 14 degrees by wavelength.	40
3.9	Transmission of ThO ₂ on polyimide film at 93 degrees by wavelength.	41
3.10	Reflection of ThO ₂ on silicon by wavelength.	42
3.11	Transmission through our sample as a function of y position. The high transmission on the left side of the plot is through the uncoated polyimide window. The lower transmission on the right side of the plot is through the polyimide film coated with thorium oxide. There are no places on the plot where transmission is uniform as y is varied.	43
3.12	Reflection of ThO ₂ on polyimide at 20 degrees as a function of wavelength. Each data set was taken with a different set of filters and order sorters in order to get the desired wavelength. In this plot, reflectance does not match up as the filter set was changed, showing us that we don't know what the data means.	45
3.13	Reflection and transmission data for thorium oxide on a polyimide film at 210 Å fit simultaneously. The reflection data was not fit very well, probably due to the fact that reflectance of the film was very low, and the film was visibly warped and wavy.	46

3.14	Reflection of polimide at 126 Å as a function of sample angle. We used the fringes of interference from the back and front interfaces of the film to derive a thickness for the film.	47
3.15	Plot of χ^2 vs. thickness. Two minima can be seen, one at 220 Å and one at 280 Å.	48
3.16	A representative fit of transmission data at 120 Å.	48
3.17	δ for thorium oxide fitted from transmission data from 115 Å to 225 Å.	49
3.18	β for thorium oxide fitted from transmission data from 115 Å to 225 Å.	49
3.19	Fit of reflection of thorium oxide on silicon as a function of angle. This fit uses a thickness of 220 Å for the thorium oxide film. It is not a qualitatively good fit.	51
3.20	Fit of reflection of thorium oxide on silicon as a function of angle. This fit uses a thickness of 280 Å for the thorium oxide film. Qualitatively, it is a much better fit than the same data fit with a thickness of 220 Å for the thorium oxide film.	52
3.21	δ for thorium oxide fitted from reflectance data from 115 Å to 250 Å.	52
3.22	β for thorium oxide fitted from reflectance data from 115 Å to 250 Å.	53
3.23	A comparison of δ values obtained by fitting reflection data and values obtained by fitting transmission data.	54
3.24	A comparison of β values obtained by fitting reflection data and values obtained by fitting transmission data.	54
3.25	A comparison of β values obtained by fitting transmission data with an unfixed δ and then with a fixed δ obtained by fitting reflectance data.	55

Chapter 1

Introduction

1.1 Interest in the Extreme Ultraviolet and Thorium based mirrors

The extreme ultraviolet (EUV), $100-1000 \text{ \AA}$, has been increasing in importance in recent years as its applications have increased. One of the most important applications of EUV wavelengths is in computer chip lithography. The computer industry is rapidly approaching the limit of the size of features that can be fabricated with current optical lithography technology. Using EUV wavelengths of $110-130 \text{ \AA}$ would allow lithography of smaller, faster, and more efficient circuits that operate at lower temperatures. For biological and medical research, smaller images can be taken with EUV light than can be taken with optical wavelengths, due to the fact that light diffracts around an object that is on the order of its wavelength. Also, in the range of $20-40 \text{ \AA}$ wavelengths, water is reasonably transparent while carbon is opaque. Thus samples can be imaged without complex dehydration and staining procedures. EUV astronomy is also a blossoming field. Helium, the second most prevalent element in the universe, has both an atomic and an ionic emission line in the extreme ultraviolet and thus can be imaged in this wavelength region. For all of these developing applications, it is necessary not only to have well-designed and well-researched optics, but highly

reflective materials to make processes accurate and efficient. For this reason, the optical properties of new materials must be measured in this region for use in thin film optics design.

1.2 Project Background

One of the main reasons why technology used for visible light optics has not become available in the extreme ultraviolet is the lack of reliable optical constants in this region. For several years, Brigham Young University's Thin Films Research Group has been studying uranium as a possible candidate for high-reflectance in the EUV. Theoretically, uranium's high density and large number of electrons would make it a good reflector in this region. Although uranium has been shown to be very reflective, it has many problems associated with its application, namely, oxidation. When exposed to oxygen, pure uranium will oxidize in a matter of minutes to one of several states including UO_2 , U_2O_5 , UO_3 , and often two or more of these states will coexist in the same sample. These oxidation states have significantly different optical properties than elemental uranium. Because the exact state of the material in a uranium film is not known, it is nearly impossible to predict how it will reflect.¹

Thorium-based films provide a possible alternative to uranium films in that they also may be more reflective than commonly used EUV reflectors, but they avoid problems with multiple oxidation states because thorium only has one oxidation state, ThO_2 . Thorium should be a good reflector in the EUV because it also has large numbers of electrons, and although its density (11.7 g/cm^3) is considerably less than that of pure uranium (19.3 g/cm^3), its density is very similar to that of uranium dioxide (10.96 g/cm^3).

The Center for X-ray Optics at Lawrence Berkeley National Labs² calculates theoretical reflectance using extrapolation between measured points along with atomic scattering factor estimates. For compounds, CXRO weights elemental scattering

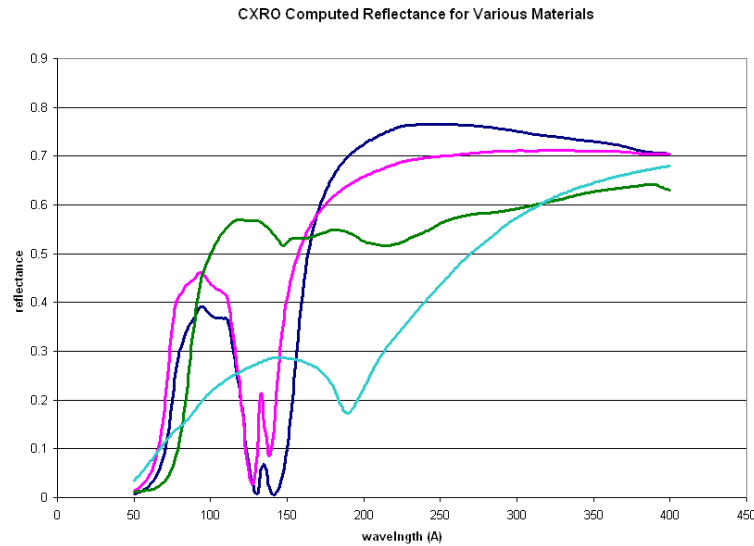


Figure 1.1: CXRO computed reflectance as a function of wavelength at 15° . Although gold and nickel are two commonly used reflector materials in this region, thorium based mirrors may be more reflective at wavelengths longer than 160 \AA .

factors according to their relative abundances. In Figure 1.1, CXRO reflectance data for thorium metal and thorium oxide is plotted with the data of two commonly used reflectance materials in this region, gold and nickel. According to CXRO, thorium-based films may be more reflective than gold or nickel films for wavelengths longer than 160 \AA . In order to take advantage of its potentially high reflectance, it is necessary to accurately determine the optical constants for thorium based films in the EUV.

1.3 Theory

1.3.1 Optical Constants

In order to design multilayer optics using a certain material, we need to know how that material will reflect, transmit, and absorb different wavelengths of light. Reflec-

tion, transmission, and absorption in a material are governed by the way the material behaves when placed in an electromagnetic field. In matter, Maxwell's equations are given by

$$\nabla \cdot \mathbf{D} = 0 \quad (1.1)$$

$$\nabla \times \mathbf{E} = -\frac{\partial \mathbf{B}}{\partial t} \quad (1.2)$$

$$\nabla \cdot \mathbf{B} = 0 \quad (1.3)$$

$$\nabla \times \mathbf{H} = \frac{\partial \mathbf{D}}{\partial t} \quad (1.4)$$

An amorphous material, as is our case, can be approximated as a linear, homogeneous material where

$$\mathbf{D} = \epsilon \mathbf{E} \quad (1.5)$$

$$\mathbf{H} = \frac{1}{\mu} \mathbf{B} \quad (1.6)$$

and ϵ and μ do not vary point to point. In this case, Maxwell's equations become

$$\nabla \cdot \mathbf{E} = 0 \quad (1.7)$$

$$\nabla \times \mathbf{E} = -\frac{\partial \mathbf{B}}{\partial t} \quad (1.8)$$

$$\nabla \cdot \mathbf{B} = 0 \quad (1.9)$$

$$\nabla \times \mathbf{B} = \mu \epsilon \frac{\partial \mathbf{E}}{\partial t} \quad (1.10)$$

These equations are almost identical to Maxwell's equations for electromagnetic waves in vacuum, with ϵ_0 and μ_0 replaced with ϵ and μ . Thus the speed of an electromagnetic wave in a material is given by

$$v = \frac{1}{\sqrt{\epsilon \mu}} = \frac{c}{n} \quad (1.11)$$

where n , the index of refraction of the material is given by

$$n = \sqrt{\frac{\epsilon \mu}{\epsilon_0 \mu_0}}. \quad (1.12)$$

For most materials, μ is approximately equal to μ_0 , making

$$n \approx \sqrt{\frac{\epsilon}{\epsilon_0}} = \sqrt{\epsilon_r} \quad (1.13)$$

where ϵ_r is the dielectric constant.³ n is typically a complex number, and so is defined as

$$n = 1 - \delta + i\beta \quad (1.14)$$

where δ is the real part of the index of refraction and β is the imaginary part of the index of refraction or the absorption coefficient. Once this index of refraction of a material is known, it is relatively easy to calculate the reflection and transmission of s and p polarized light from a perfect boundary using the boundary conditions

$$\epsilon_1 E_1^s = \epsilon_2 E_2^s \quad (1.15)$$

$$B_1^s = B_2^s \quad (1.16)$$

$$E_1^p = E_2^p \quad (1.17)$$

$$\frac{1}{\mu_1} B_1^p = \frac{1}{\mu_2} B_2^p. \quad (1.18)$$

These equations are the origin of the Fresnel coefficient equations

$$f_{s,m} = \frac{q_m - q_{m-1}}{q_m + q_{m-1}} \quad (1.19)$$

$$f_{p,m} = \frac{n_{m-1}^2 q_m - n_m^2 q_{m-1}}{n_{m-1}^2 q_m + n_m^2 q_{m-1}} \quad (1.20)$$

$$g_{s,m} = \frac{2q_m}{q_{m-1} + q_m} \quad (1.21)$$

$$g_{p,m} = \frac{2n_{m-1}q_m}{n_m q_{m-1} + n_{m-1}q_m} \quad (1.22)$$

where q is given by

$$q_m = \sqrt{n_m^2 - \cos^2 \theta_m}, \quad (1.23)$$

θ is the angle of incidence measured from grazing, and m is the m^{th} interface in the

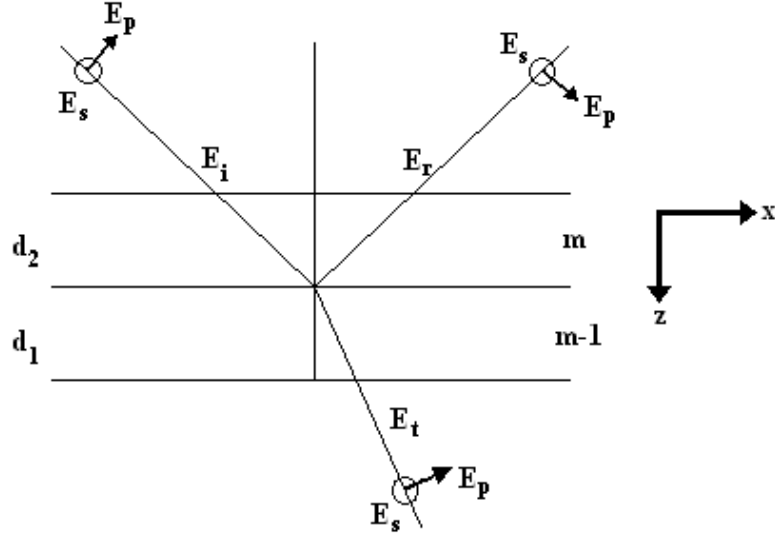


Figure 1.2: The geometry used to calculate theoretical reflectance and transmittance.

multilayer. In the visible region, the index of refraction is the preferred description of the optical properties of a material, while in the x-ray region, the preferred description is the atomic scattering factor

$$f = f_1 + if_2 \quad (1.24)$$

The relations between these two quantities are as follows

$$\delta = \frac{a_0 \lambda^2 \rho}{2\pi A} f_1 \quad (1.25)$$

$$\beta = \frac{a_0 \lambda^2 \rho}{2\pi A} f_2 \quad (1.26)$$

where λ is the vacuum wavelength, ρ is the density, and A is the atomic weight. These relations are derived by calculating both quantities for a free electron gas and are general descriptions of the way materials behave in the x-ray region if f_1 is the number of free electrons per atom. In the EUV electrons are not free, so the complex atomic scattering factor describes the "effective" number of free electrons

for an atom. The values of f_1 and f_2 are obtained by finding the number of electrons needed to obtain the right δ and β in equations 1.21 and 1.22.⁴

1.3.2 Experimentally determining optical constants

1.3.2.1 Reflectance and transmittance measurements

Experimentally determining the optical constants of a material requires taking reflectance or transmittance measurements off of a film and working backwards with the Fresnel coefficient equations to find δ and β . Reflectance and transmittance measurements are taken using a monochromator (see figure 1.3). In a monochromator, one wavelength of light is isolated using gratings, filters, and pinholes and is then either reflected off of or transmitted through a film. For reflectance, the film and the detector are rotated through a theta-two theta scan, giving a data set of reflected intensity as a function of sample angle. For transmittance, the detector is held fixed while the film is rotated around 90 degrees.

1.3.2.2 Fitting

Once reflection measurements are taken, we fit the data to the Parratt recursion relation⁵⁶

$$r_{s,m} = C_m^4 \frac{f_{s,m} + r_{s,m-1}}{1 + f_{s,m} r_{s,m-1}} \quad (1.27)$$

$$r_{p,m} = C_m^4 \frac{f_{p,m} + r_{p,m-1}}{1 + f_{p,m} r_{p,m-1}} \quad (1.28)$$

where

$$C_m = \exp\left(-\frac{i\pi q_m d_m}{\lambda_m}\right) \quad (1.29)$$

d_m is the thickness of the m th layer and λ_m is the wavelength in the layer. From these values, reflection in any layer is given by

$$R_s = |r_{s,m}|^2 \text{ and } R_p = |r_{p,m}|^2 \quad (1.30)$$

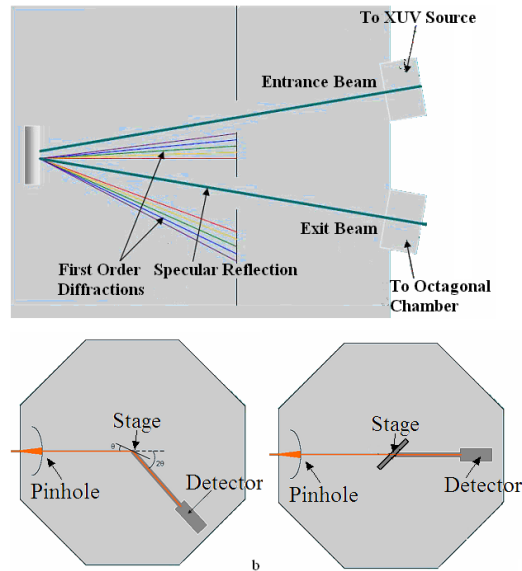


Figure 1.3: a) a monochromator b) reflection measurement c) transmission measurement

We solve this equation by realizing that at the substrate $C_1 = 1$ because this layer is essentially infinite. We can then recursively find the reflection at each interface. For transmittance, we use a matrix formulation to calculate transmission at each interface. The implementation of this procedure will be discussed in the next section. Our fitting program uses a least-squares fitting technique to find the set of parameters that were most likely to have created the data set. The fitting library we used to analyze our data, MINUIT,⁷ was developed at CERN in Switzerland. Our interface, a program called matfit, defines the function and supplies the data to this library.

1.3.2.3 Transmission Calculation using Matrices

Here is a sample of my code:

```
/**Computes the reflectance and transmission of a stack at an
angle
```

```

* theta(in degrees) using matrices.
* @param theta angle (in degrees)
* @param stack Vector of layer objects describing the stack.
* Be sure to include the vacuum layer (with a thickness
* of zero) and substrate(be sure to include thickness if you want
* transmission data. If not, thickness=0).
* The first layer in the stack should be the substrate.
* Has been checked against the test program eariler in
* this class and against the old way of computing reflectance
* (i.e. the Parratt formula).
* Returns t, but could return both r and t.
*/
public double refl_trans(double theta,Vector stack){
    double kx;
    Vector klayer = new Vector();
    Complex n1,n2,k1,k2;
    Complex Fs21,Fs12,Gs21,Gs12;
    Complex Fp21,Fp12,Gp21,Gp12;
    Complex C1,C2;
    Complex Rs=new Complex(0);Complex Rp=new Complex(0);
    Complex Ts=new Complex(0);Complex Tp=new Complex(0);
    Matrix As=new Matrix(1,0,0,1);
    Matrix Ap=new Matrix(1,0,0,1);
    Matrix Bs=new Matrix(1,0,0,1);
    Matrix Bp=new Matrix(1,0,0,1);
    double r; double t;

```

k_x is the x component of the vacuum wave vector k .

```
kx=k*Math.cos(theta*Math.PI/180);
```

Gets n from the input stack and computes the z component of k in layer i .

```
for(int i=0; i<stack.size(); i++){
    Complex n=((layer)(stack.get(i))).n;
    n=(sqr(n.times(k)).minus(sqr(kx))).sqrt();
    klayer.add(n);
}
for (int i=0;i<stack.size()-1;i++){
    k2=(Complex)klayer.get(i+1);
    k1=(Complex)klayer.get(i);
    n2=sqr(((layer)(stack.get(i+1))).n);
    n1=sqr(((layer)(stack.get(i))).n);
```

F_{s21} is the Fresnel coefficient for s polarization giving the ratio of the amplitudes of the reflected wave to the incident wave in layer 2.

```
Fs21 = (k2.minus(k1)).over(k1.plus(k2));
Fs12 = (k1.minus(k2)).over(k2.plus(k1));
```

G_{s21} is the Fresnel coefficient for s polarization giving the ratio of the amplitudes of the transmitted wave in layer 1 to the incident wave in layer 2.

```
Gs21 = new Complex(2,0).times(k1).over(k2.plus(k1));
Gs12 = new Complex(2,0).times(k2).over(k1.plus(k2));
```

Fp21 and Fp12 give the reflection coefficients for p polarization. Gp21 and Gp12 give the transmission coefficients for p polarization.

```

Fp21 =
    (sqr(n1).times(k2).minus(sqr(n2).times(k1))).over(
        sqr(n2).times(k1).plus(sqr(n1).times(k2)));
Fp12 =
    (sqr(n2).times(k1).minus(sqr(n1).times(k2))).over(
        sqr(n1).times(k2).plus(sqr(n2).times(k1)));
Gp21 =
    new Complex(2, 0).times(
        (sqr(n2).times(k1)).over(
            sqr(n1).times(k2).plus(sqr(n2).times(k1))));
Gp12 =
    new Complex(2, 0).times(
        (sqr(n1).times(k2)).over(
            sqr(n2).times(k1).plus(sqr(n1).times(k2))));

```

The coefficient C_m gives the phase and amplitude modulation of the field while propagating through the half layer m .

$$C_m = \exp \frac{ik_z h}{2} \quad (1.31)$$

where h is the thickness of the layer.

```

C1 = ((new Complex(0, (((layer)(stack.get(i)))
    .thick)/2)).times(k1)).exp());
C2 = ((new Complex(0, (((layer)(stack.get(i+1)))

```

```

        .thick)/2)).times(k2)).exp();

    As = Am(Gs21,Gs12,Fs21,Fs12,C1,C2);
    Bs = As.times(Bs);

    Ap = Am(Gp21,Gp12,Fp21,Fp12,C1,C2);
    Bp = Ap.times(Bp);
}

Rs = (Bs.A12).over(Bs.A22);
Ts = new Complex(1, 0).over(Bs.A22);

Rp = (Bp.A12).over(Bp.A22);
Tp = new Complex(1, 0).over(Bp.A22);

r = sFrac * sqr(Rs.mag()) + pFrac * sqr(Rp.mag());
t = sFrac * sqr(Ts.mag()) + pFrac * sqr(Tp.mag());

return t;
}

private static Matrix Am(Complex gpm,Complex gmp,Complex fpm,
    Complex fmp,Complex cm,Complex cp){

    Complex A11 = (gpm.times(cm).times(cp))
        .minus(fpm.times(fmp.times(cm.times(cp))))).over(gmp));
    Complex A12 = fpm.times(cp).over(gmp.times(cm));

```

```

Complex A21 = new Complex(-1,0).times(fmp).times(cm)
    .over(gmp.times(cp));
Complex A22 = new Complex(1,0).over(cm.times(cp).times(gmp));
return new Matrix(A11,A12,A21,A22);
}

```

1.3.3 Roughness

Reflectance from a boundary is calculated by assuming that film boundaries are infinitely sharp or transition infinitely fast. In reality, film boundaries have a finite width. Contributions from different depths within a boundary will add amplitudes with different phases, resulting in a different reflectivity than expected. The three types of roughness we will be dealing with in this paper are large-scale roughness, small-scale roughness, and interdiffusion. Large-scale roughness is defined as roughness that is much larger than the wavelength of light we are using. Large-scale roughness results in non-specular or diffuse scattering, that is, the reflected angle is no longer equal to the incident angle of light. Large-scale roughness will decrease the measured reflectance of a surface because at the expected angle, a rough surface will only reflect a fraction of the light that a smooth surface will.

Accordingly, small-scale roughness is roughness that is on the order of or smaller than the wavelength of light we are using. Small-scale roughness changes the way that light interferes when it is reflected. In a perfectly smooth plane of atoms, a reflected plane wave interferes destructively at all angles except the specular angle. If atoms are displaced, however, this perfect interference is destroyed, and it is difficult to predict how light will reflect.

Interdiffusion between layers and on the surface of a film is not roughness in the typical sense of the word. However, it is still a mechanical imperfection that affects

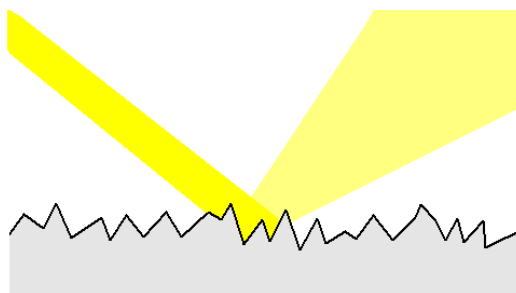


Figure 1.4: Large scale roughness results in diffuse scattering, decreasing the reflectivity of the surface at the specular angle.

optical properties of our materials. Interdiffusion has to do with the fact that in reality, there is no such thing as an infinitely fast jump from one material to another. Since we are only dealing with monolayer films and we don't believe our sample is diffusing with our substrate, the interdiffusion we will deal with is surface oxidation of our sample.

1.3.4 Accepted methods of accounting for roughness

In the literature⁸⁹, the accepted methods of accounting for roughness are scalar correction factors. There are two prevalent scalar factors used, the Debye-Waller factor and the Nevot-Croce factor.^{10 11} Both of these factors are derived using a Fourier transform method. Let's assume that the reflectivity of a boundary is smeared out to a Gaussian distribution of width sigma around the ideal boundary.

$$r(z) = \frac{r_0}{\sigma\sqrt{2\pi}} \exp(-z^2/(2\sigma^2)) \quad (1.32)$$

where r_0 is the amplitude reflectivity of a perfectly smooth surface and σ is the RMS roughness of the surface. This sort of Gaussian distribution is obtained by adding a large number of different periodic amplitudes with random phases. Debye and Waller justified this distribution by picturing the boundary as a random superposition

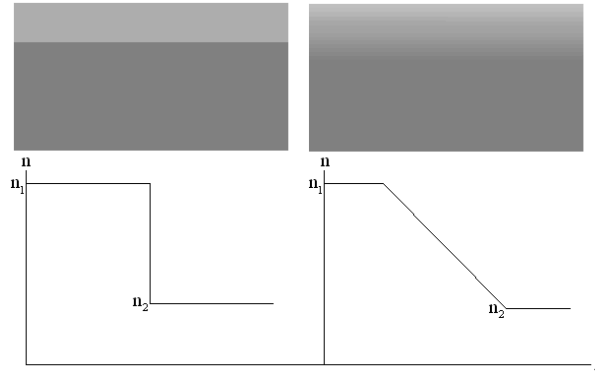


Figure 1.5: Interdiffusion of layers. In an ideal multilayer, composition changes infinitely fast from one material to another. In real multilayers, interfaces have a finite width. left: an infinitely sharp boundary right: a diffuse boundary

of lattice vibrations. Taking the Fourier transform of this boundary gives us the amplitude reflectivity of

$$r(q) = r_0 \exp(-q^2 \sigma^2) / 2 \tag{1.33}$$

with q being the momentum transfer

$$q = \frac{4\pi}{\lambda} n \sin(\theta) \tag{1.34}$$

where λ is the vacuum wavelength, n is the index of refraction, and θ is measured from grazing. The reflected intensity is then given by

$$R(q) = R_0 \exp(-q^2 \sigma^2) \tag{1.35}$$

$$= R_0 \exp\left(\left(\frac{-2\pi * m\sigma}{\lambda} n \sin(\theta)\right)^2\right) \tag{1.36}$$

This factor $\exp(-q^2 \sigma^2)$ is called the Debye-Waller factor. In this derivation we have assumed that the momentum transfer q is constant within the material transition. That is, this factor does not take into account how the changing index of refraction changes the propagation angle as the light refracts. Nevot and Croce produced a

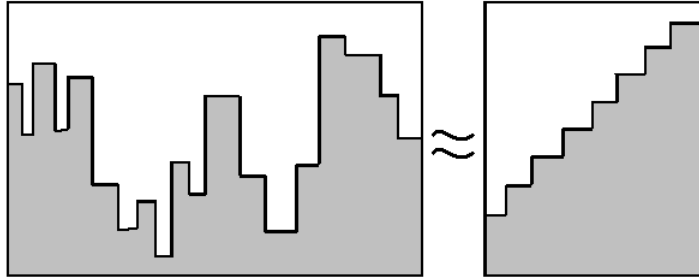


Figure 1.6: Surface roughness in a film can be approximated as a series of steps in density from vacuum to the material.

factor that was a correction to the Debye-Waller factor that replaced q^2 with the geometric average $q_1 q_2$. Thus the Nevot-Croce factor is given by

$$R(q) = R_0 \exp(-q_1 q_2 \sigma^2) \quad (1.37)$$

There is another method of accounting for roughness called the finite differences approximation. In equations 1.21 and 1.22 we can see that in the atomic scattering factor model, δ and β are proportional to the material density. Thus if the density is varying in the transition between two materials, we can say that its optical constants are behaving in approximately the same way. A varying transitional density may come about by interdiffusion between two layers, surface oxidation, or surface roughness (see Figure 1.6). In surface roughness, fluctuating height of the surface is similar to interdiffusion with vacuum. Because of this dependence on density, an imperfect transition into a material can be approximated as a series of perfect layers whose index of refraction varies functionally. The zeroth order finite difference approximation is a linear variation in optical constants (see Figure 1.7).

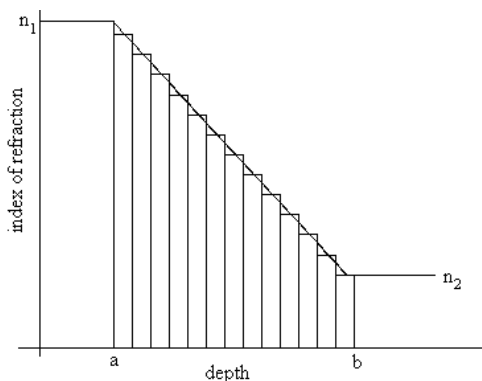


Figure 1.7: A schematic of the finite differences approximation. A gradient in the index of refraction between points a and b is approximated as a finite number of layers whose indices of refraction vary linearly from n_1 to n_2 .

1.3.5 Project Focus

This paper will focus on finding the optical constants of thorium oxide. I will discuss the problems we went through with thorium films including roughness and oxidation and how we decided to move to thorium oxide films. I will then discuss the processes we went through to determine the optical constants of thorium oxide and the problems with the data and results we have obtained.

1.3.6 Film Deposition

The thorium films used in this project were deposited using RF sputtering with a base pressure of 6×10^{-7} Torr and a sputtering pressure of 5 mTorr. The thorium oxide films used in this project were reactively sputtered using RF sputtering with a base pressure of 9.7×10^{-7} Torr, an oxygen partial pressure of 1.3 mTorr, and a sputtering pressure of 8.3 mTorr. With our thorium oxide samples, we had some compositional inconsistencies run to run, but the particular samples we used were determined by X-ray Photoelectron Spectroscopy to be homogeneous.

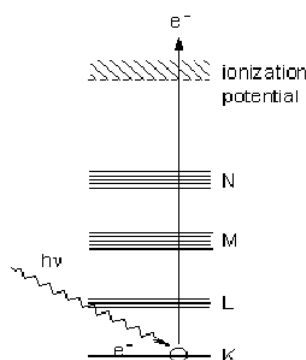


Figure 1.8: The photoelectric effect

1.3.7 Characterization theory

1.3.7.1 X-ray Photoelectron Spectroscopy (XPS)

X-ray photoelectron spectroscopy (XPS) uses the photoelectric effect to determine the composition of a sample (see figure 1.8). The sample is irradiated with either aluminum or magnesium $K\text{-}\alpha$ x-rays and the energy of the ejected electrons are measured. The difference between the energy of these ejected electrons and the incident x-rays is the characteristic binding energy of the irradiated material. The measured energies can tell us the relative abundance of elements in a sample. Depth profiling can be achieved using this technique by interspersing compositional analysis with argon ion sputtering. In this way, data points can be taken of composition as a function of depth.

1.3.7.2 Atomic Force Microscopy (AFM)

Atomic force microscopy (AFM) measures surface characteristics of a sample directly by dragging a cantilever over the surface and measuring displacement using a laser (see Figure 1.9).

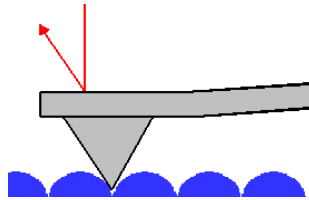


Figure 1.9: AFM tip

1.3.7.3 X-ray Diffraction (XRD)

In x-ray diffraction (XRD), copper K- α radiation ($\lambda = 1.5406 \text{ \AA}$) is reflected off of a sample near grazing. This scattering can be approximated as Bragg diffraction.

$$m\lambda = 2d \sin \theta \quad (1.38)$$

where m is the diffraction order, λ is the wavelength of light in the material, d is the thickness of the film, and θ is the incident angle. The thickness of a film can be estimated from XRD data by using the difference in angle between interference peaks in this equation.

Chapter 2

Roughness

Effectively modelling reflection and transmission data in order to determine the optical constants of a material requires the ability to accurately calculate the scattering of radiation off of that material, a feat that necessitates an understanding of interfaces and a robust theory of the interaction of radiation with nonideal surfaces. It is simple to calculate the reflectance and transmittance of radiation from an ideal interface using Fresnel's equations and employing a few simple assumptions, such as the assumption that the interface is perfectly smooth. However, in practice it is easily seen that these assumptions do not describe reality, and are often not a good enough approximation for our purposes. Thus, one must attempt to describe and account for these imperfections in our optics.

Our group was interested in determining the optical constants of thorium as previously discussed. Although all of the calculations made in this chapter were performed using data from a thorium sample, we hope that the same calculations could be employed for any sample. With that in mind, we first began fitting reflectance data for a single layer of thorium on a silicon substrate at 150 \AA with our program that assumed an ideal interface, both superficially smooth and with ideal interfacial tran-

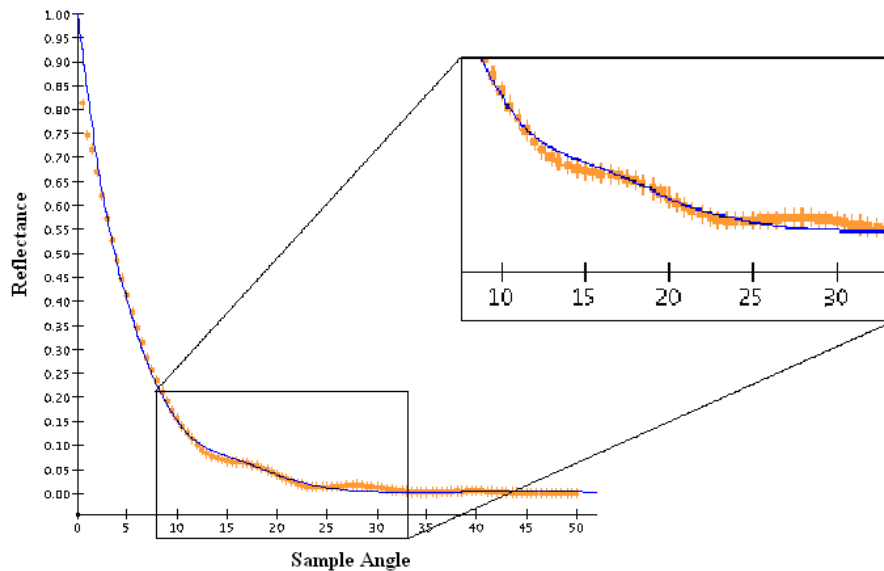


Figure 2.1: Reflectance data for a single layer of thorium on a Silicon substrate at 150 \AA . Along the x-axis is plotted angle, and along the y-axis is plotted reflectance. The fit assumes smooth boundaries and abrupt interfaces. The inset shows the poor-ness of the fit at middle angles (10-30 degrees).

sitions. These fits were not very good. Referring to Figure 2.1 we can see that our fit (the blue line) is not a very good representation of the data (the orange dots). This is especially true in the middle angles from 10 to 30 degrees where the data has some very interesting oscillations that the fit does not follow. These oscillations are the most important part of the data because they are what make the reflectance data for thorium unique. Thus if we can't fit the oscillations well, we won't know that we have the correct fit and thus the correct optical constants.

Because of these poor fits, we are prompted to ask the question, what in our sample is not being described well in our program? We hypothesized surface roughness as well as surface oxidation. This hypothesis was supported by AFM data as well as

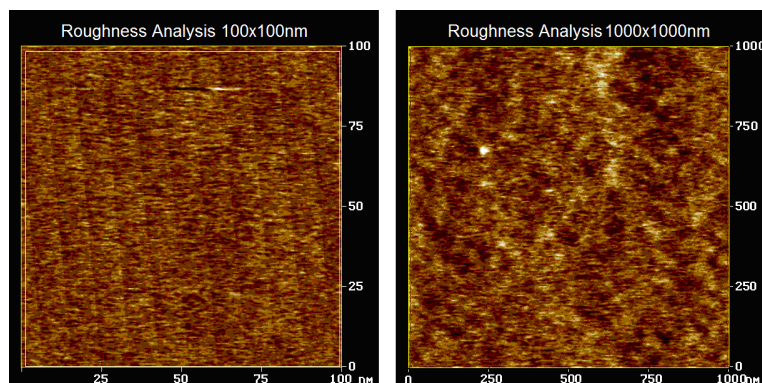


Figure 2.2: Atomic force microscopy profiles of thorium at two length scales: 100x100nm and 1000x1000nm. At the 100x100nm length scale, RMS roughness equals 3.6nm. At the 1000x1000nm length scale, RMS roughness equals 4.3nm.

XPS depth profile data. Our program assumed both a perfectly smooth surface and perfectly abrupt boundaries. Our goal then was to incorporate roughness into our program, and thus fit our data more accurately.

2.1 Characterization of Roughness

In order to characterize the magnitude and length-scale of our surface roughness, we used AFM to find the root mean squared (RMS) roughness of our sample at two length scales and the power spectral density function of our sample. On a 100nm by 100nm length scale, we found our RMS roughness to be 3.6 nm. This tells us that our small-scale roughness is of significant magnitude. On a 1000nm by 1000nm scale, we have an RMS roughness of 4.3 nm. This tells us that we also have large-scale roughness of significant magnitude (Figure 2.2). A power spectral density plot tells us the relative amounts of roughness we have at each length scale. From Figure 2.3 we can see that we have the highest density of roughness from 40 to 80 nm, which is on the order of the wavelength of light we are using (150 \AA). This tells us that

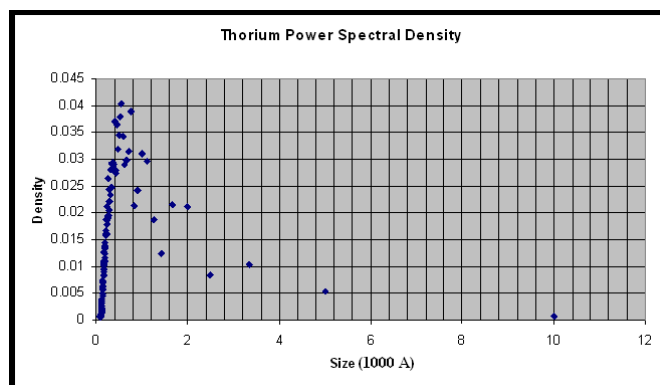


Figure 2.3: Power spectral density plot of thorium. The highest density of roughness occurs in the range from 40 to 80 nm, small-scale roughness.

although the magnitude of our large-scale roughness is significant, we don't have a significant amount of it. Thus we know that we should concern ourselves only with small-scale roughness, which is significant in both amount and magnitude. In order to characterize the surface oxidation of our sample, we did an XPS depth profile of the surface. We found that our sample oxidized nearly linearly for about 50 \AA (see Figure 2.4). The thorium-silicon edge in our plot gives us an idea about the resolution of this technique because we assume that there is no interdiffusion between our sample and the substrate.

2.2 Problems with Characterization

After characterizing our sample using AFM and XPS, we wanted to determine how far we could trust our data. One major concern we had was AFM measurements where the size of the roughness was on the order of the size of the tip used to measure it.

As can be seen from Figure 2.5, a large tip cannot characterize high-frequency roughness accurately. In order to see how great an effect this had on the data given

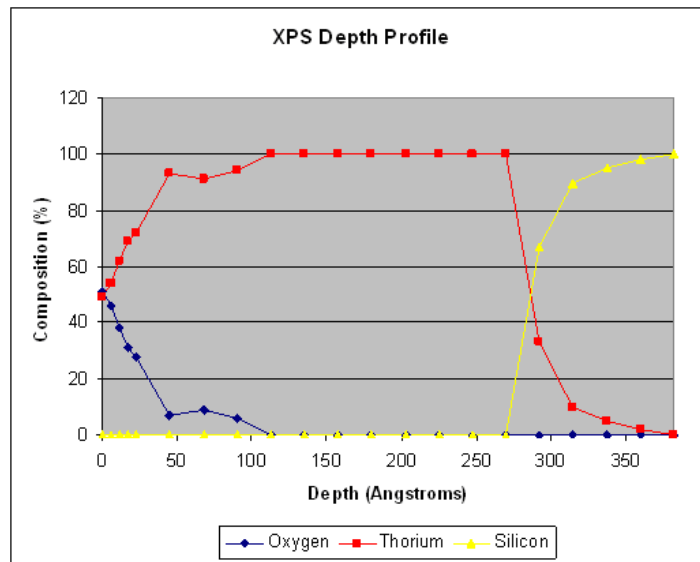


Figure 2.4: X-ray photoelectron spectroscopy depth profile of Thorium. The surface of the sample has oxidized nearly linearly for about 50 Å. The Thorium-Silicon edge gives as an idea of the resolution of this technique because we assume that this boundary is sharp.

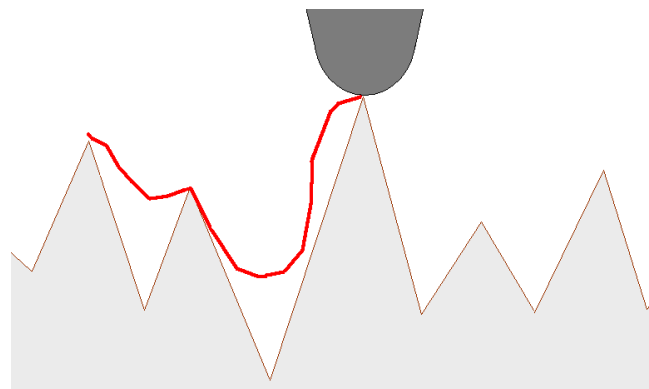


Figure 2.5: An AFM tip that is on the order of the size of the roughness being measured cannot characterize roughness accurately.

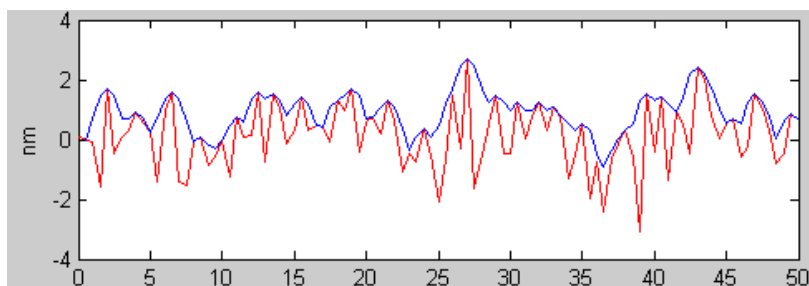


Figure 2.6: A rough surface approximated by Gaussian random numbers (red line). The blue line is the surface as measured by the AFM tip. The RMS roughness of the surface is 1.03 nm while the RMS roughness detected by the tip was 0.23 nm.

to us by AFM, we modeled it in Matlab. We generated a surface, dragged a tip of non-zero width across it, and computed the RMS roughnesses and power spectral densities, one of the real surface and one of the surface as it was detected by the tip. Our first approximation of our surface was a Gaussian random distribution, with mean 0 and standard deviation 1. A characteristic example is displayed in Figure 2.6. The red line represents the surface, while the blue line represents the surface as detected by the tip. For this surface, we found that the real RMS roughness was 1.03 nm while the RMS roughness reported by the finite tip was 0.23 nm. For this surface, the real RMS roughness of the surface is four times the RMS roughness reported by the tip.

The power spectral density reported by the tip is similarly skewed. Figure 2.7 shows a plot of the power spectral density of the surface (red) and the surface detected by the tip (blue). The power spectral density of the surface is flat because the roughness on the surface is random, point to point. For this surface, the tip not only fails to detect high frequency roughness on the surface, it actually detects more low frequency roughness than is actually present.

This model of the surface is probably not completely accurate because on real

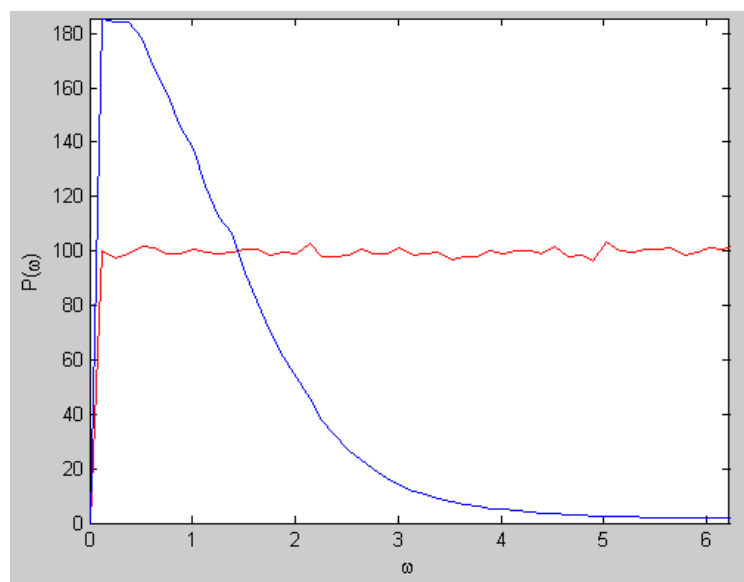


Figure 2.7: The power spectral density of the surface (red) and the surface detected by the tip (blue). For this surface, the tip not only fails to detect high frequency roughness on the surface, it actually detects more low frequency roughness than is actually present.

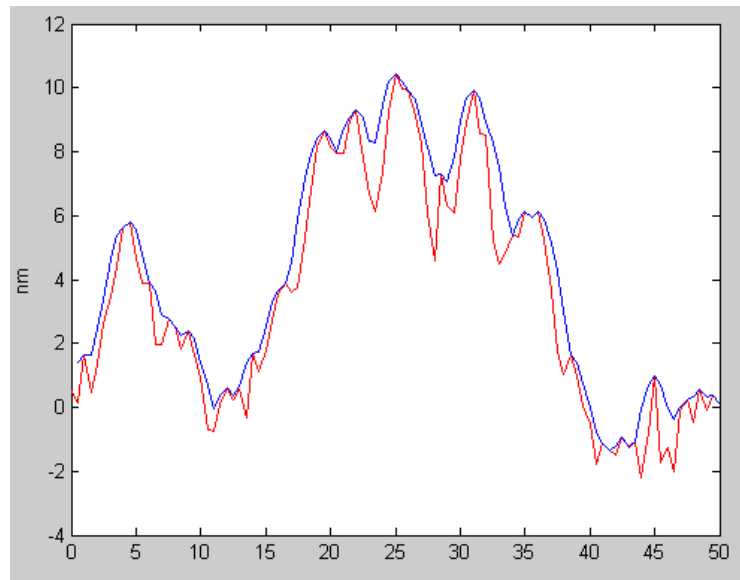


Figure 2.8: A rough surface approximated by correlated Gaussian random numbers (red line). The blue line is the surface as measured by the AFM tip. The RMS roughness of the surface is 1.49 nm while the RMS roughness detected by the tip was 1.33 nm.

surfaces each point is not independent of the points around it; there is some amount of correlation point to point. The next approximation of our surface was a surface where each point was random around the point previous to it. A characteristic example is displayed in Figure 2.8. The red line represents the surface, while the blue line represents the surface as detected by the tip. For this surface, we found that the real RMS roughness was 1.49nm while the RMS roughness reported by the finite tip was 1.33. For this surface, the real RMS roughness of the surface is only 1.12 times the RMS roughness reported by the tip.

Similarly, the power spectral density reported by the tip for this surface corresponds to the actual power spectral density of the surface (see Figure 2.9). They

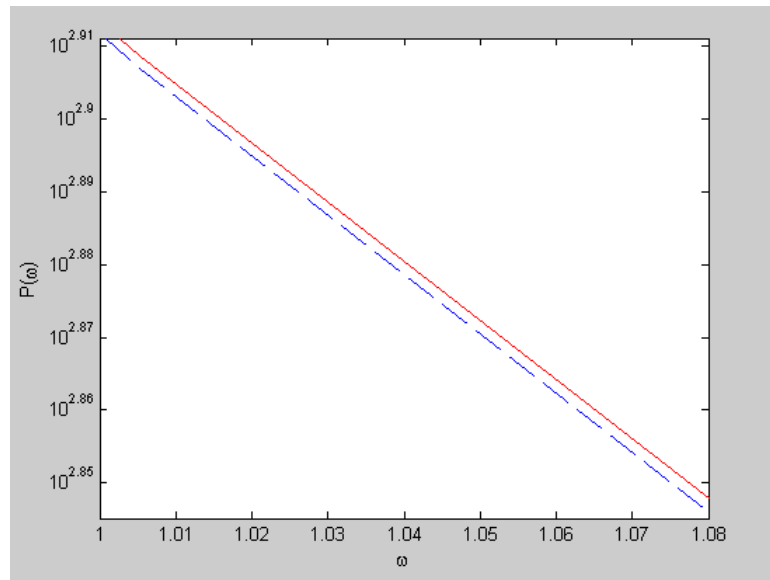


Figure 2.9: The power spectral density of the surface (red) and the surface detected by the tip (blue). For this surface, the PSD of the real surface and the surface detected by the tip match almost identically.

have the same shape, but the surface detected by the tip has less roughness than the actual surface universally. If the power spectral densities were normalized, the two plots would match almost identically.

These two models represent the two extremes in the possibilities of the correlation of our surface. Our surface is probably neither completely uncorrelated nor completely correlated, but somewhere in between. Our third approximation for our surface was derived by taking a completely uncorrelated surface and at each point multiplying it by a Gaussian of width σ . By changing the value of σ , the surface can be given different length scales of correlation. As we change this value, we can see the power spectral densities of the surface and of the surface reported by the tip move closer to one another.

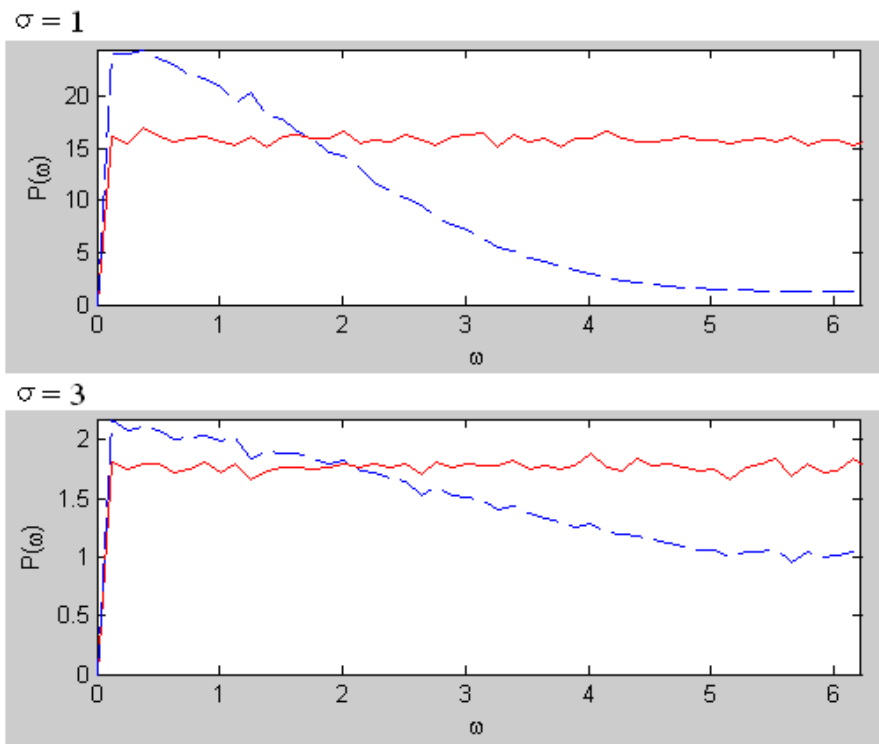


Figure 2.10: The power spectral density of the surface (red) and the surface detected by the tip blue. As the length scale of correlation gets longer, the PSD measured by the tip gets closer to the actual PSD of the surface.

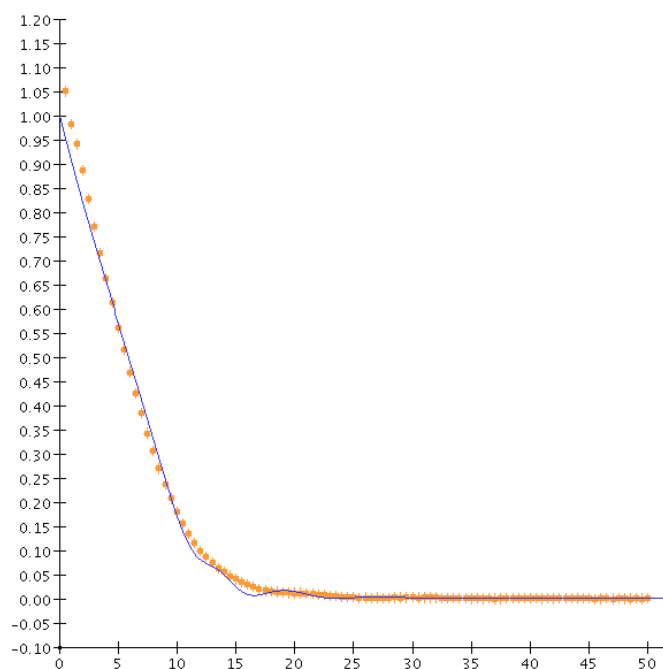


Figure 2.11: Fit of thorium reflection data after correction using the Debye-Waller factor. The factor improved the fit only at low angles.

2.3 Accounting for Roughness

We analyzed the efficacy of methods of accounting for roughness by correcting our data and then fitting it to see how the fit improved. First we corrected our data using the Debye-Waller scalar correction factor. The fit was still not very good, especially at our important middle angles, but the fit did improve at low angles (see Figure 2.11). Although the fit was not drastically better, we know that the correction was a step in the right direction because our data at zero degrees was closer to 100%.

The fit after correction using the Nevot-Croce factor was vastly improved (see Figure 2.12). The fit was excellent at low angles and much better at high angles. The fit at middle angles was improved, but still not very good.

We employed the method of finite differences, approximating the 50 \AA transition

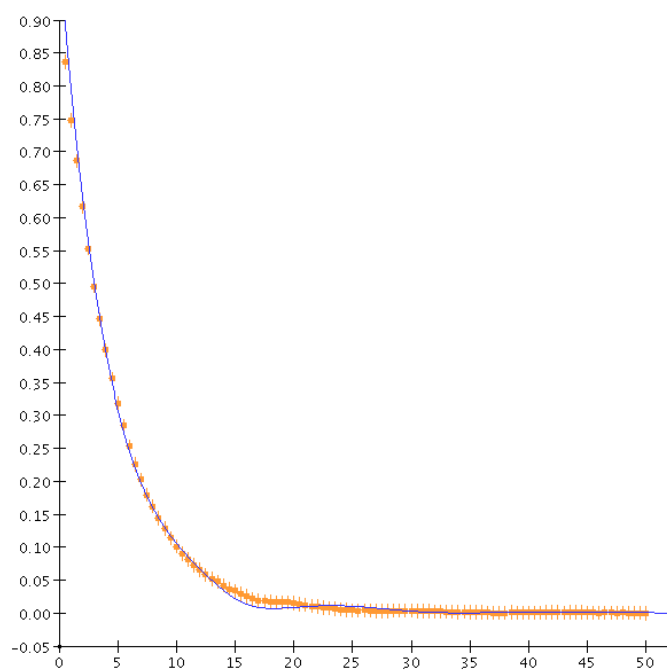


Figure 2.12: Fit of thorium reflection data after correction using the Nevot-Croce factor. The factor improved the fit significantly at low and high angles.

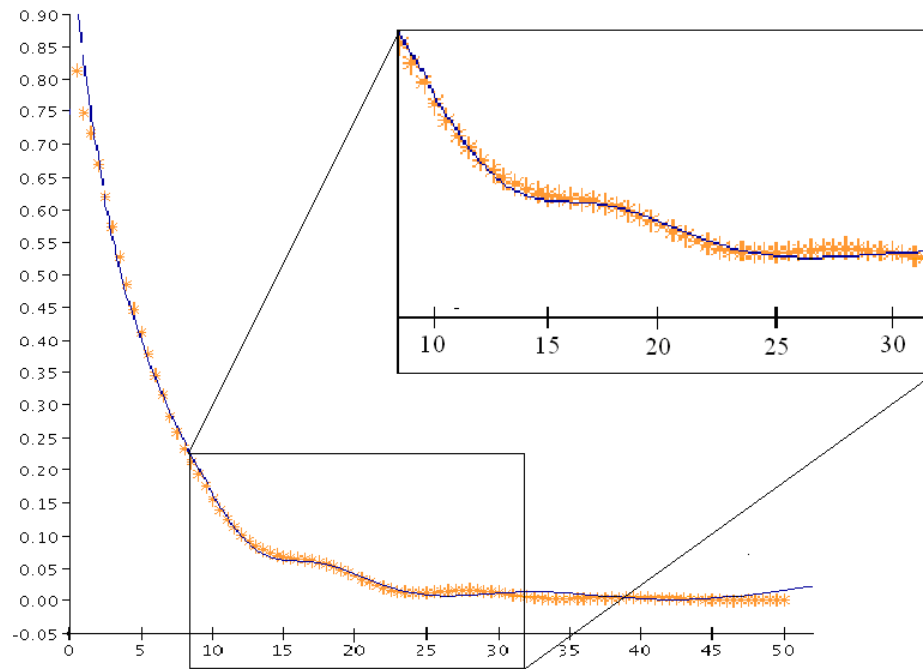


Figure 2.13: Fit of thorium reflection data with a 50 Angstrom transition layer approximated as five 10 Angstrom layers whose indices of refraction varied linearly. The approximation improved the fit significantly at low and middle angles.

layer of oxidation and roughness in thorium with five perfect layers of 10 \AA each whose index of refraction varied linearly between them. The fit we got was excellent at low and middle angles (see Figure 2.13). This was the zeroth order approximation for this type of a correction. A good area for future research would be a non-linear variation of optical constants or a trapezoidal or polynomial rather than rectangular fit.

Chapter 3

Finding the Optical Constants of Thorium Oxide

3.1 Reflectance and Transmittance Measurements

To find the optical constants of thorium oxide, we took both reflectance and transmittance data in order to decrease the degrees of freedom in our fitting program. We deposited thorium oxide on two substrates: a silicon wafer and half of a thin membrane of polyimide provided by Moxtek¹² leaving the other half of the film uncoated. Measurements were taken at the Advanced Light Source at Lawrence Berkeley National Lab¹³. The ALS is a synchrotron light source which accelerates electrons moving at relativistic velocities using magnetic fields. These accelerating particles emit photons at essentially continuous wavelengths from $0.2\text{\AA} - 0.6\text{ mm}$. As electrons emit light and also as experience collisions, they lose energy. Thus, over the space of a few hours, the beam current decreases and our reflectance measurements must be normalized to this beam current. This normalization procedure will be discussed shortly. Our reflectance and transmittance measurements were taken at beamline 6.3.2, a beamline with a bend magnet source and an energy range of 50-1300eV

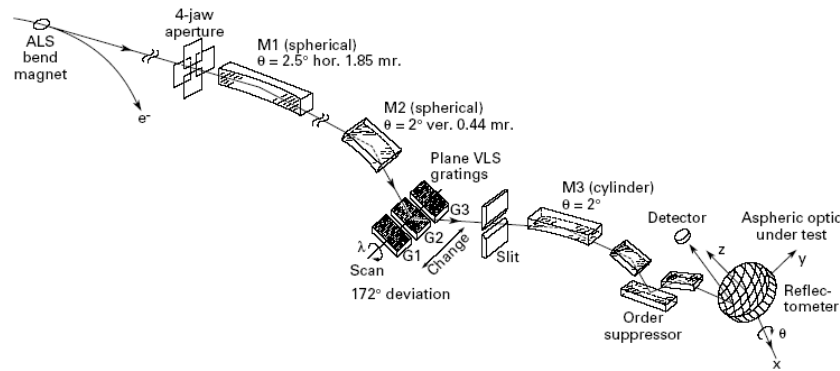


Figure 3.1: A schematic layout of ALS beamline 6.3.2.

$(9.5 - 250 \text{ \AA})$. A schematic of the beamline is shown in Figure 3.1. The beamline's configuration provides high spectral resolution and purity, beginning with a spherical mirror which focuses the beam onto one of three variable-line-spaced gratings designed to correct for aberrations of the mirror (200 l/mm, 600 l/mm, and 1200 l/mm). Then the beam passes through a series of filters and a triple-mirror configuration intended to suppress higher order light. The wavelength is varied by rotating the grating with respect to a fixed exit slit. The configuration's resolving power ($E/\Delta E$) is 7000, and the beam size at the sample is $300 \times 10 \mu\text{m}$. The beam intensity at the sample for the 600 l/mm grating and the 1200 l/mm grating is given in Figure 3.2. The beam intensity for the 200 l/mm is not shown. The resolution of the monochromator for each of the three gratings is shown in Figure 3.3. The filters used in this beamline setup are Al ($0.3 \mu\text{m}$), Si ($0.3 \mu\text{m}$), B ($0.5 \mu\text{m}$), C ($2 \mu\text{m}$), Ti ($0.6 \mu\text{m}$), Cr ($0.55 \mu\text{m}$), Co ($0.33 \mu\text{m}$), and Cu ($0.64 \mu\text{m}$). Table 3.1 gives the filter, order sorter mirror and angle, and grating used to achieve pure wavelengths in a given range. The grating, filter, and order sorter sets overlap at the edges of the wavelength ranges they are meant to produce. This becomes a problem when measurements made with two different filter

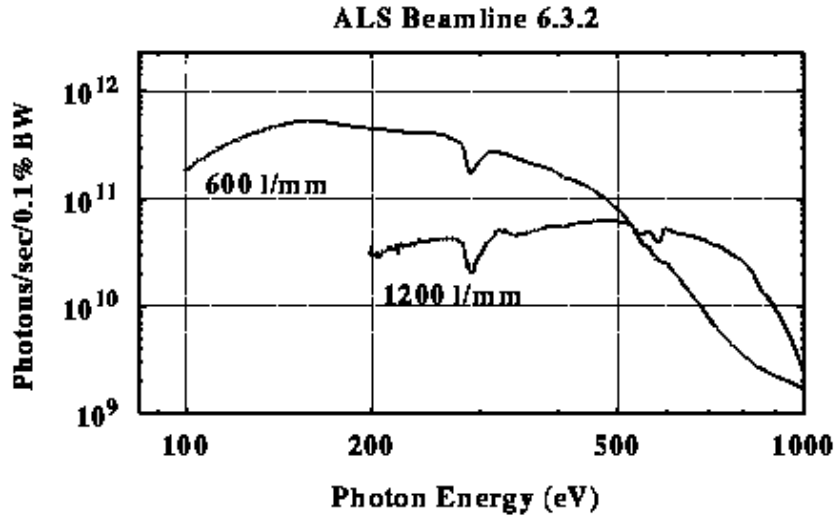


Figure 3.2: Beam intensity at the sample position.

<i>Wavelength Range (\AA)</i>	<i>Grating (l/mm)</i>	<i>Filter, Order Sorter, Angle</i>
20-28	600	Cr, Ni, 6.2°
27-48	600	Ti, Ni, 6.2°
44-68	600	C, Ni, 8°
66-88	600	B, C, 6.2°
84-116	200	B, C, 8°
110-140	200	Be, C, 8° or 10°
124-188	200	Si, C, 10°
172-250	200	Al, C, 10°

Table 3.1: Grating, filter, and order sorters used to achieve spectral purity for the given wavelength range.

CHAPTER 3. FINDING THE OPTICAL CONSTANTS OF THORIUM OXIDE³⁶

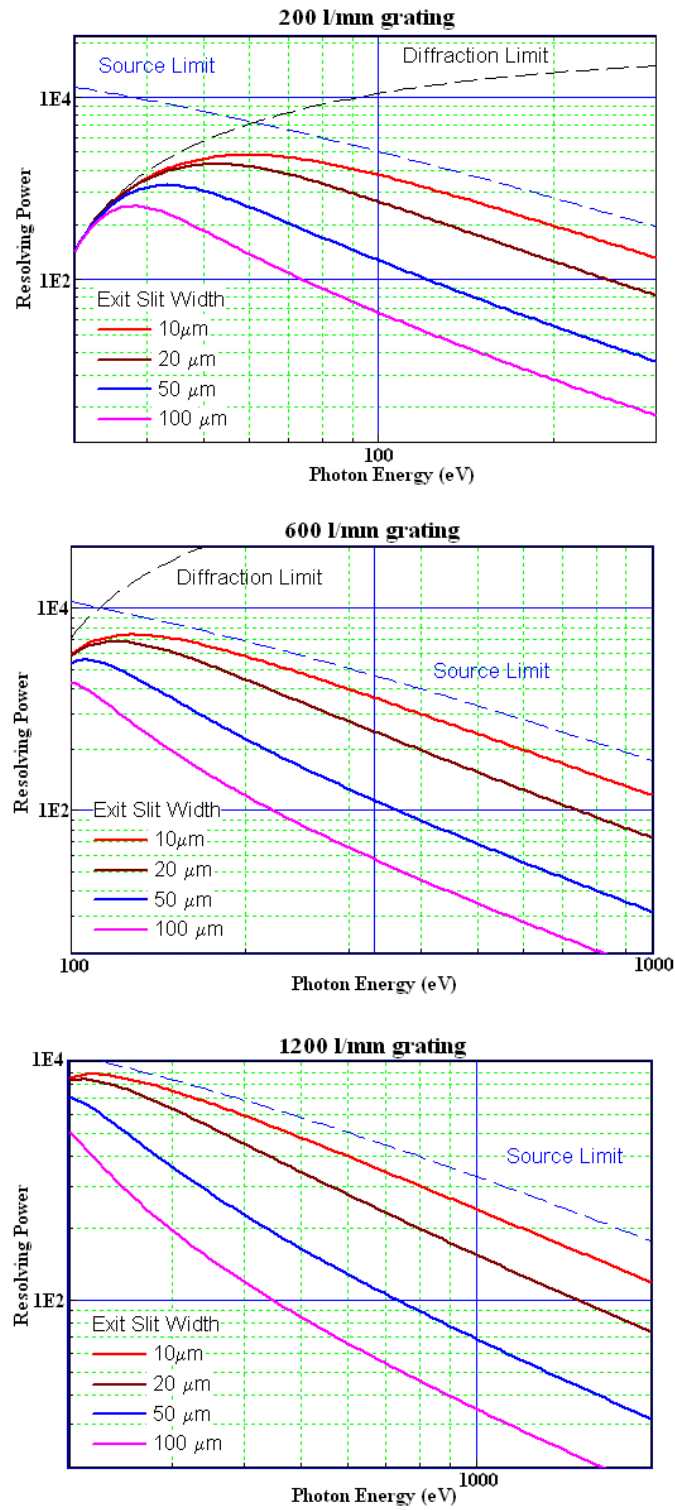


Figure 3.3: Monochromator resolution.

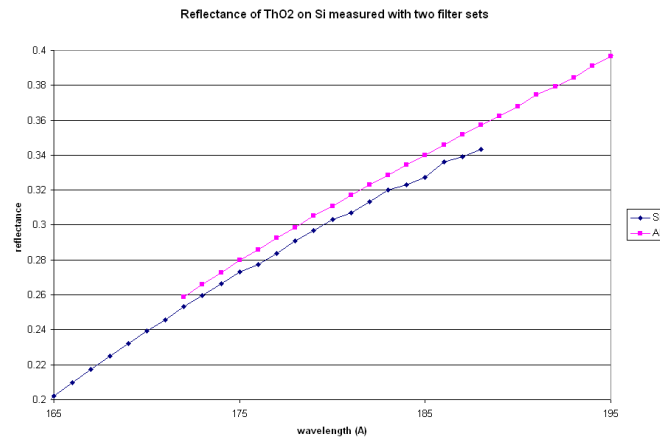


Figure 3.4: Reflectance of ThO_2 on Si measured with two filter sets at 14° . The two measurements disagree by as much as 0.013.

sets do not overlap. We experienced this problem repeatedly in the region where the silicon and aluminum filters overlap, the region from $172 - 188 \text{ \AA}$. Figure 3.4 shows reflectance of ThO_2 on silicon from $165 - 195 \text{ \AA}$. The two measurements never agree, and are dissimilar by as much as 0.013. To find out which of these filter sets gave us better data, we placed a second grating inside the beamline's reflectometer at the sample stage. At a fixed wavelength, we rotated this grating with respect to a fixed detector. For a spectrally pure beam we should see a sharp spike at one grating angle. What we saw is depicted in Figure 3.5. The inset shows spectral impurities in the wavelength produced by the silicon filter set. From this data, we know that when the silicon and aluminum filter sets give us conflicting data, we should believe the aluminum filter set data.

The beamline's reflectometer allows sample movement in the x , y , z , and θ directions where x and y are parallel to the sample plane, z is perpendicular to the sample plane, and θ is measured from grazing (see Figure 3.6). The translation motors can

CHAPTER 3. FINDING THE OPTICAL CONSTANTS OF THORIUM OXIDE³⁸

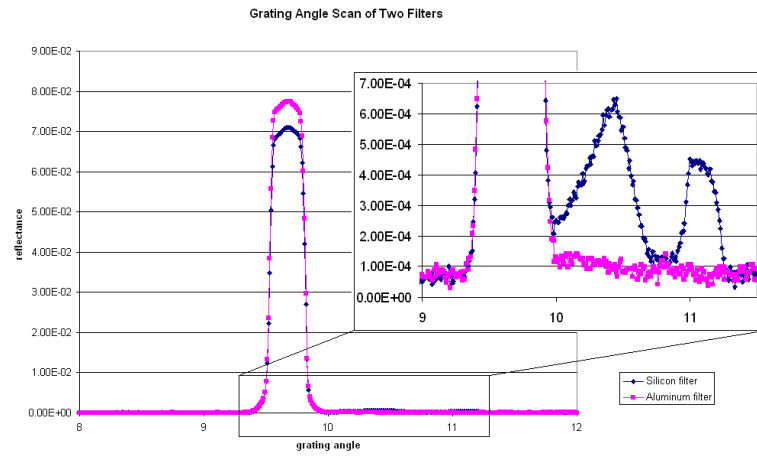


Figure 3.5: A second grating was placed at the sample stage and rotated with respect to a fixed detector. The two data sets were taken with two different filter sets with a wavelength of 180 \AA . The inset shows spectral impurities in the wavelength produced by the silicon filter set.

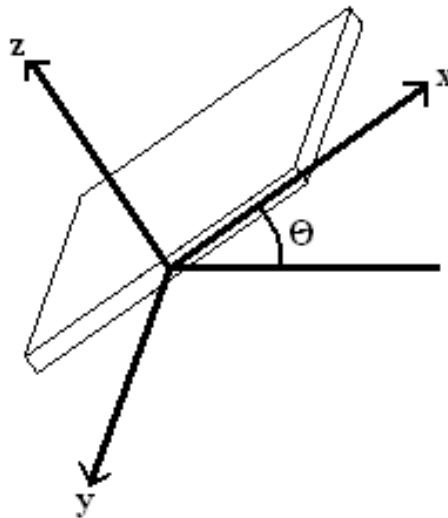


Figure 3.6: Sample stage axis specifications for beamline 6.3.2 reflectometer.

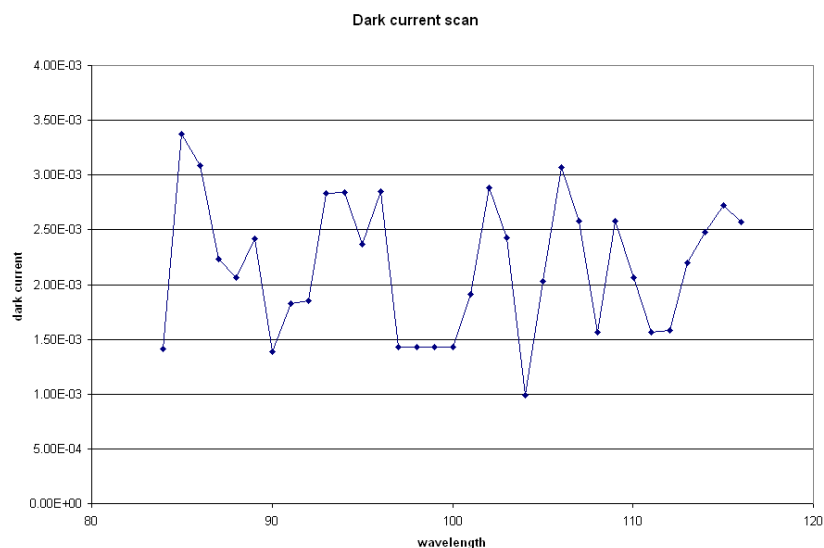


Figure 3.7: A typical dark current scan taken as a function of wavelength.

position to within $1\mu m$ and the angular motor can position to within 0.002° . The detector in the reflectometer that we used for our measurements was a photodiode. A problem we have had to deal with repeatedly while using this detector is dark current, that is, signals measured by the photodiode when no beam is on it. These signals are procured from many sources: electrical noise, visible light leakage from outside the chamber, etc. This dark current is an absolute error, and so we have to worry about it a lot more when our signal is small. Typical dark currents usually fluctuate randomly, however, dark current has been shown in some cases to depend on wavelength, sample angle, or time of day. They are usually around $1 - 5 \times 10^{-3}$. A typical scan is shown in Figure 3.7. This scan was taken as a function of wavelength, even though no light is supposed to be getting into the chamber. This scan seems to be fairly random.

Normalization procedure for our scans is as follows: first we normalize our re-

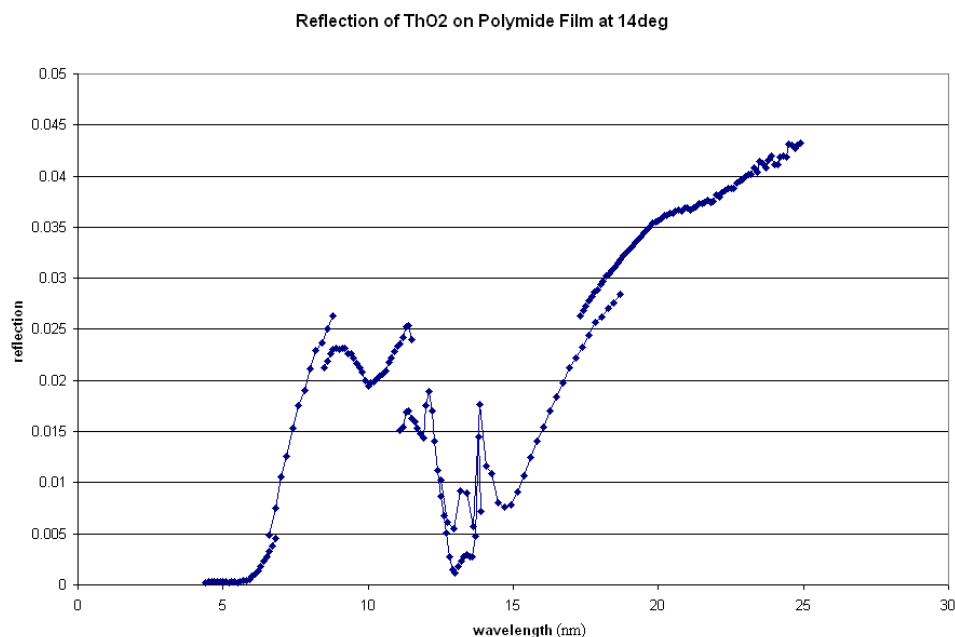


Figure 3.8: Reflection of ThO₂ on polyimide film at 14 degrees by wavelength.

reflectance measurements to the beam current. Second, we normalize our I_0 scan to the beam current. An I_0 scan is a wavelength scan taken with no sample, just the beam going straight into the detector. We then subtract the dark current (also normalized to the beam current) from both our reflectance measurement and our I_0 measurement. We then divide our reflectance measurement by our I_0 measurement in order to obtain percentage reflectance.

3.2 Reflectance and Transmittance Data

Figures 3.8 and 3.9 show plots of reflection as a function of wavelength and transmittance as a function of wavelength for the sample deposited on polyimide film. Figure 3.10 shows a plot of reflection as a function of wavelength for the sample deposited on silicon. From the sample on polyimide film we measured both transmittance and reflectance although reflectance was only around three percent. One problem we had

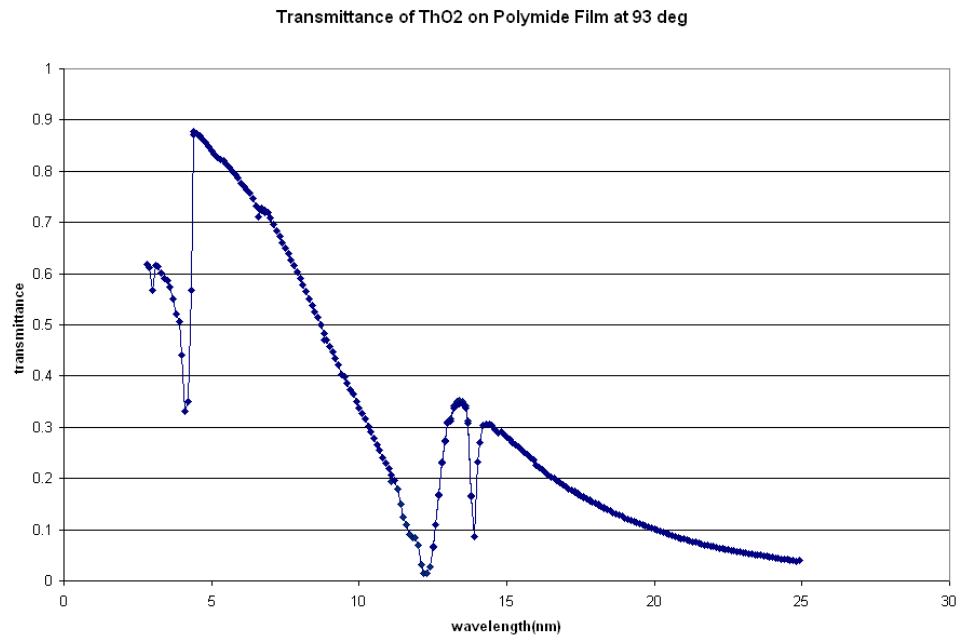


Figure 3.9: Transmission of ThO₂ on polyimide film at 93 degrees by wavelength.

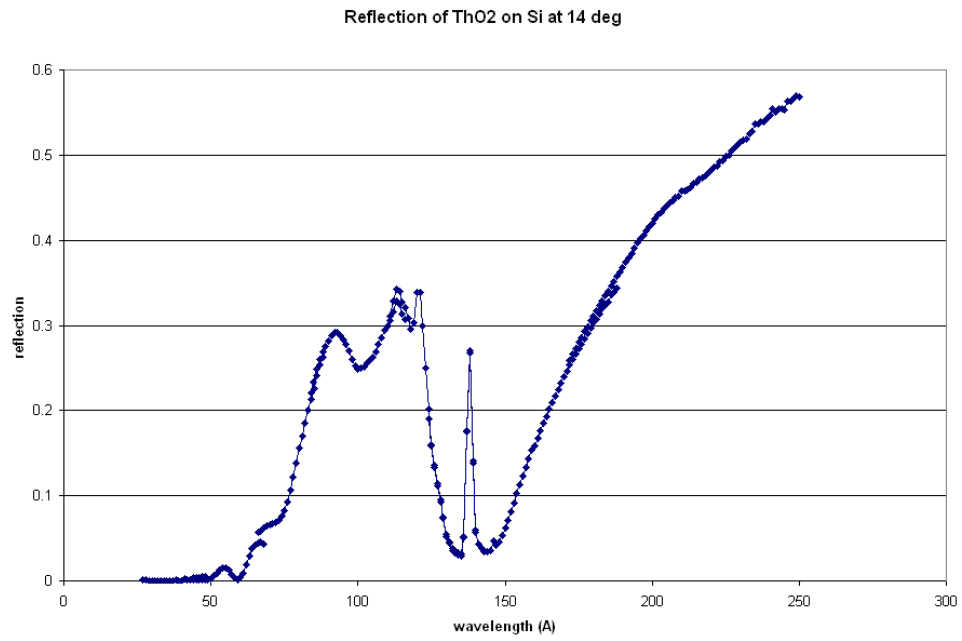


Figure 3.10: Reflection of ThO₂ on silicon by wavelength.

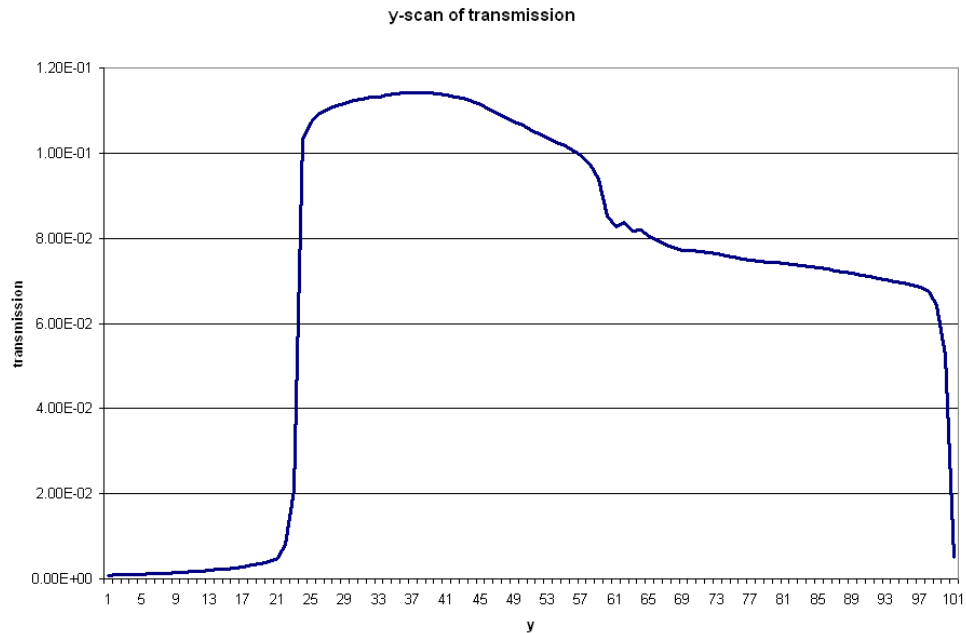


Figure 3.11: Transmission through our sample as a function of y position. The high transmission on the left side of the plot is through the uncoated polyimide window. The lower transmission on the right side of the plot is through the polyimide film coated with thorium oxide. There are no places on the plot where transmission is uniform as y is varied.

with these samples was that the substrate membrane was so thin that the films buckled and warped when they were deposited on. The films were visibly wavy, making it tricky to get good measurements. There were no places where the transmission looked uniform while doing a y -scan of transmission (see Figure 3.11). This tells us that something in our sample is changing across the surface. It is most likely something about the polyimide window itself rather than the coating because the transmission on the uncoated side of the window is also varying as y -position is changed. Because transmittance was up around 50% this small variation across the film did not affect our

transmission measurements very much. However, this variation and the wavy nature of the film did affect our reflection measurements, both because of our extremely small signal measurements and because waviness affects grazing measurements much more than normal-incidence measurements. Our small signals in reflection measurements were also affected significantly by the dark current, which was on the order of 5% of our total signal. The reflectance scans we took did not match up when we changed order sorter and filter sets (see Figure 3.12). We have had this problem before as was previously mentioned, but never on this scale. At some wavelengths, measurements disagree by as much as 32% of total reflectance. Because of this significant mismatch, we did not know what measurements to believe.

3.3 Data Fitting

We did some simultaneous fitting of reflectance and transmittance of ThO₂ on the polyimide film in order to try and decrease the degrees of freedom in our fit. As can be seen in Figure 3.13 the transmittance data (the right side of the plot) is fit well, but the reflection data (the left side of the plot) is not. Because of the problems we had with the reflection data and because of the nature of the polyimide film, we decided to discard the reflectance data and just fit the transmittance data. We still had data from reflectance off of our sample on a silicon wafer and we could fit these two sets of data simultaneously, but this required modifications to our program that we never implemented. This would be an interesting area for future research. Since the optical constants of polyimide are unknown in this wavelength region, our fitting procedure was to fit the transmission data for the uncoated film and use the constants found there in our fit of the coated data. To find the thickness of the polyimide film, we found reflectance data off of the film that contained well-defined interference fringes due to reflection off of the front and back surfaces of the film. We used the equation

$$m\lambda = 2d \sin(\theta_1 - \theta_2) \quad (3.1)$$

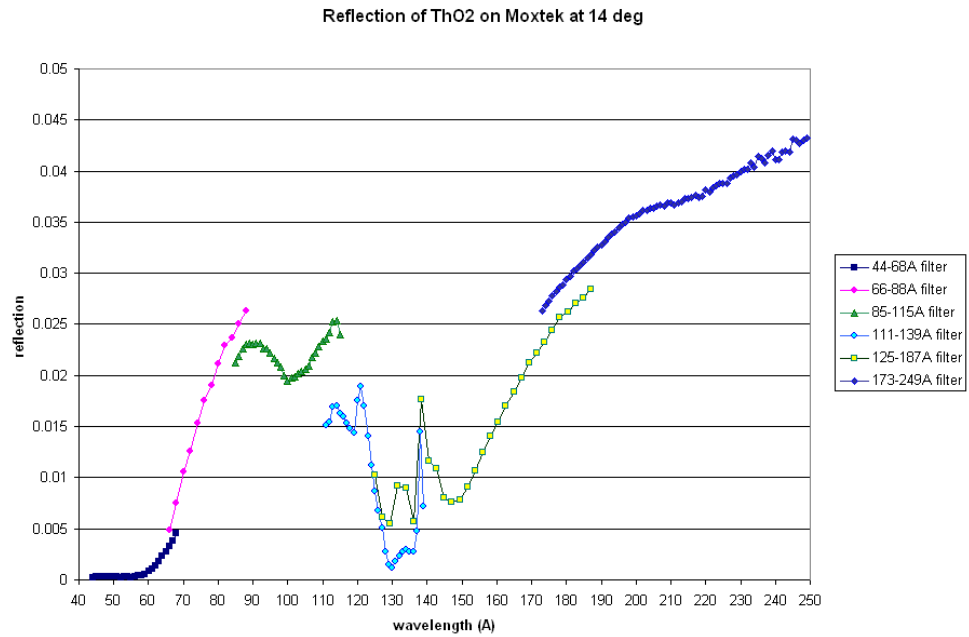


Figure 3.12: Reflection of ThO₂ on polyimide at 20 degrees as a function of wavelength. Each data set was taken with a different set of filters and order sorters in order to get the desired wavelength. In this plot, reflectance does not match up as the filter set was changed, showing us that we don't know what the data means.

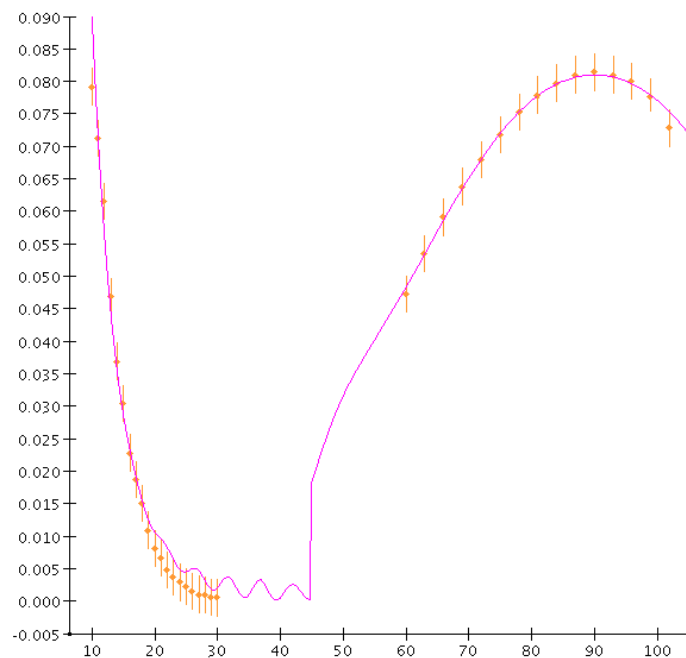


Figure 3.13: Reflection and transmission data for thorium oxide on a polyimide film at 210 \AA fit simultaneously. The reflection data was not fit very well, probably due to the fact that reflectance of the film was very low, and the film was visibly warped and wavy.

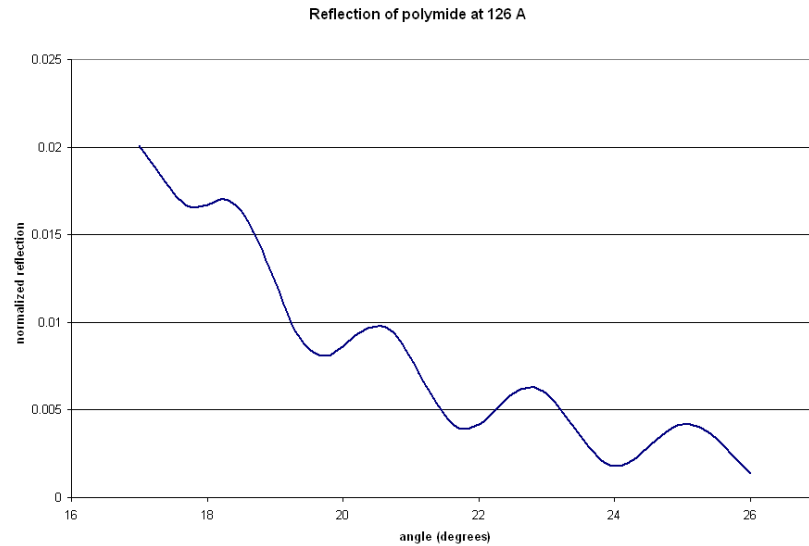


Figure 3.14: Reflection of polyimide at 126 \AA as a function of sample angle. We used the fringes of interference from the back and front interfaces of the film to derive a thickness for the film.

to find a thickness of 1603.7 \AA . The thickness of the ThO_2 film was estimated to be around 200 \AA when we sputtered it. We also took XRD data from our sample deposited on a silicon wafer at the same time as our transmission sample which we believe has the same thickness. From this measurement we obtained a thickness estimate of $220 \text{ \AA} \pm 20 \text{ \AA}$. We fit several sets of data at thicknesses ranging from 200 \AA to 300 \AA and compared the χ^2 value of the fits as is shown in Figure 3.15. We found two consistent minimums in this data, one at a 220 \AA thickness and one at a 280 \AA thickness. Because of our XRD data, we chose to do our fits with a thickness of 220 \AA . A representative fit of transmission data is shown in Figure 3.16. The optical constants derived from fits of transmittance are shown in figures 3.17 and 3.18. The values for δ given to us by these fits are all over the place and often have large

CHAPTER 3. FINDING THE OPTICAL CONSTANTS OF THORIUM OXIDE48

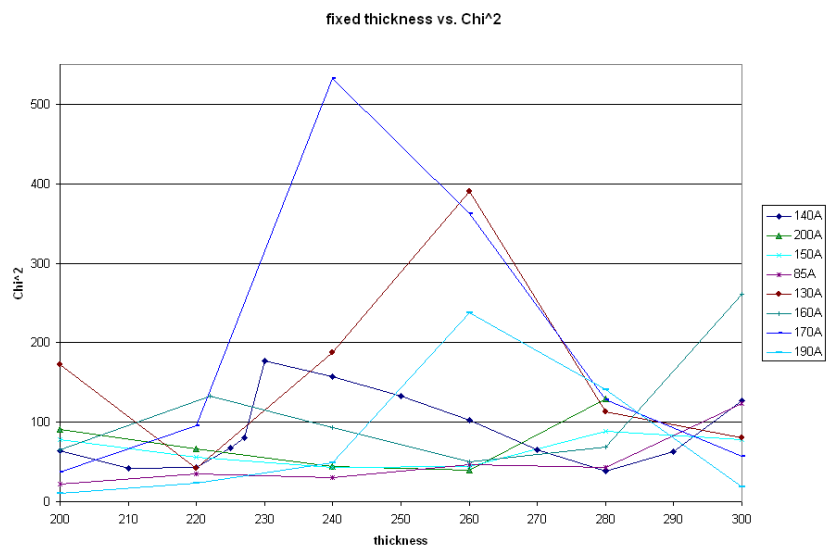


Figure 3.15: Plot of χ^2 vs. thickness. Two minima can be seen, one at 220 Å and one at 280 Å.

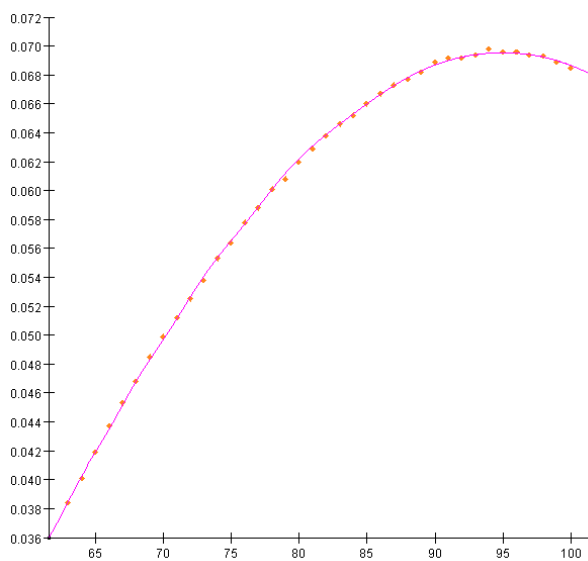


Figure 3.16: A representative fit of transmission data at 120 Å.

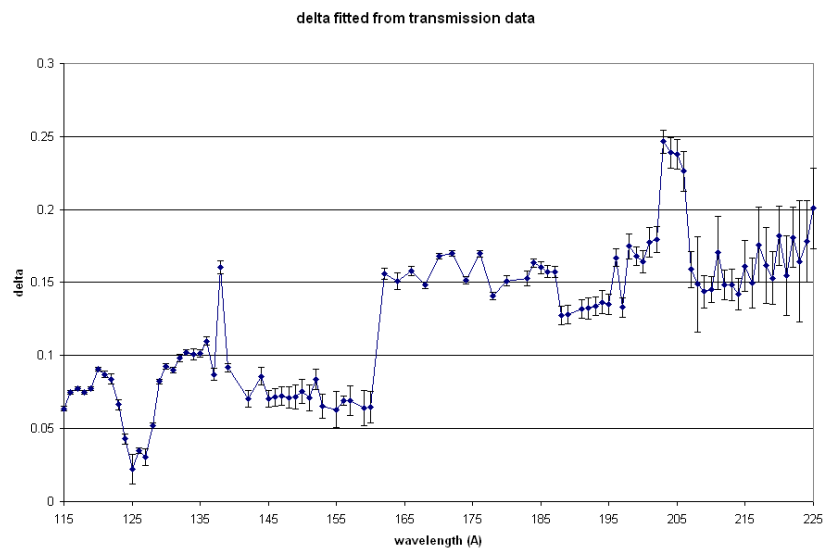


Figure 3.17: δ for thorium oxide fitted from transmission data from 115 Å to 225 Å.

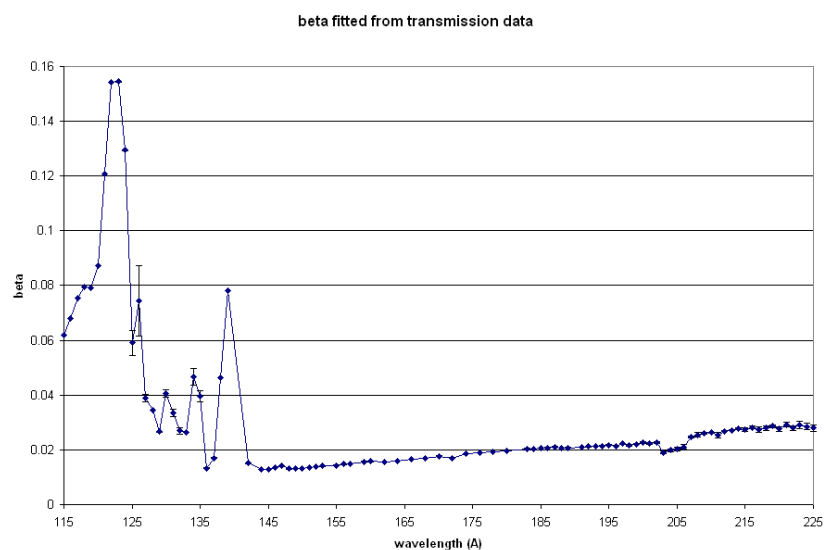


Figure 3.18: β for thorium oxide fitted from transmission data from 115 Å to 225 Å.

error bars. The values for β look more reasonable. It makes sense that δ cannot be given very accurately from transmission data. The two places δ comes into play in transmission data is in the decrease in transmitted intensity due to reflection off the front surface of the film and the change in wavelength of light from that in vacuum in the film. In this case, the film reflects very little, especially compared to the amount of light transmitted through the film at near-normal incidence. Also, δ is very small, making the amount of change in wavelength of light inside the film very small. Thus transmittance measurements depend very little on the value of δ , and so δ cannot be derived very accurately from these measurements.

Fitting reflectance data from the sample deposited on silicon raised some interesting questions. Although we had decided on a 220 Å thickness because of fitting analysis and XRD data, some of the fits of reflection data were not very good at this thickness, but qualitatively better with a thickness of 280 Å (see figures 3.25 and 3.20). The second fit was not only qualitatively better, the χ^2 value of the fit went down by a factor of 10. A thickness of 280 Å is not altogether surprising, since in our χ^2 analysis of the transmission data we found minima at both 220 Å and 280 Å. However, XRD gave us a value close to 220 Å for the thickness of the film on silicon. We had estimated the error of this value to be ± 20 Å, not ± 60 Å. One possible reason for this discrepancy is the effect of surface roughness on the film, which we failed to account for. Because of this discrepancy with the film thickness, we decided to fit the reflection data with fixed film thicknesses of 220 Å and 280 Å. The two fits gave us the values for δ and β shown in figures 3.21 and 3.22. As can be seen from Figure 3.21, the value of δ is not very dependent on the thickness of the layer. On average, the fit value of δ only changes by about 0.003 when the thickness of the film is changed from 220 Å to 280 Å. This leads us to believe that for these wavelengths and these angles, our sample is optically thick. This is a very exciting

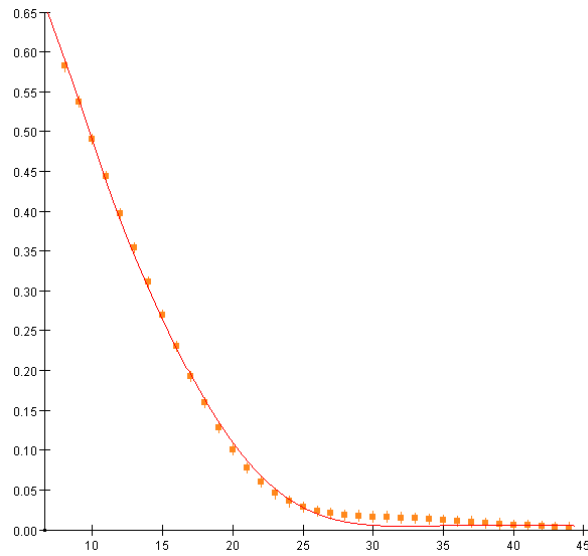


Figure 3.19: Fit of reflection of thorium oxide on silicon as a function of angle. This fit uses a thickness of 220 \AA for the thorium oxide film. It is not a qualitatively good fit.

CHAPTER 3. FINDING THE OPTICAL CONSTANTS OF THORIUM OXIDE 52

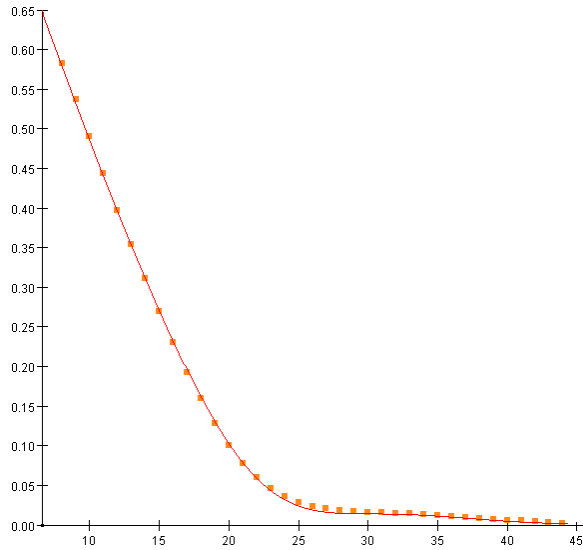


Figure 3.20: Fit of reflection of thorium oxide on silicon as a function of angle. This fit uses a thickness of 280 \AA for the thorium oxide film. Qualitatively, it is a much better fit than the same data fit with a thickness of 220 \AA for the thorium oxide film.

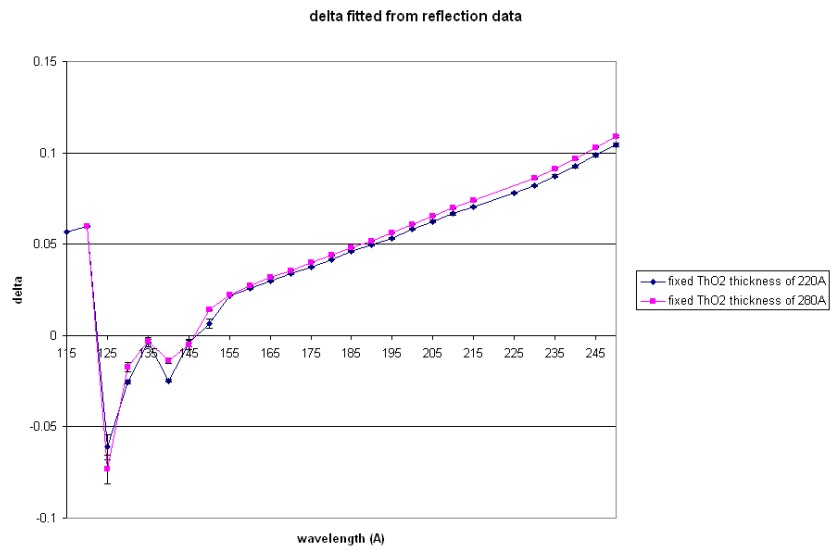


Figure 3.21: δ for thorium oxide fitted from reflectance data from 115 \AA to 250 \AA .

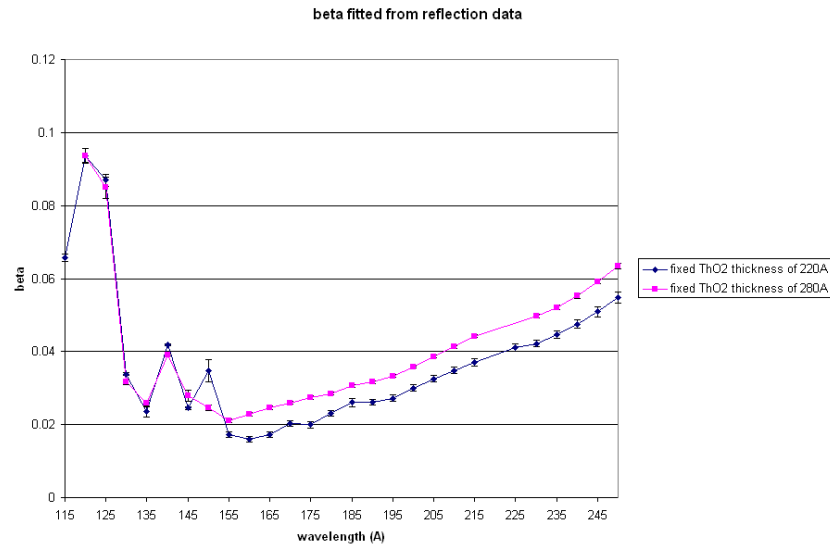


Figure 3.22: β for thorium oxide fitted from reflectance data from 115 Å to 250 Å.

conclusion because our questions concerning the real thickness of our sample do not affect our values for δ . Accordingly, as can be seen from Figure 3.22, the value of β does depend significantly on the film thickness. The value of β changes by about 0.006 when the thickness of the film is changed from 220 Å to 280 Å. This tells us that we cannot get a good value for β from reflection data unless we have a better knowledge of the thickness of the film.

Another concern with our data is that the values of δ and β fit from transmission and reflection data do not match up as can be seen in figures 3.23 and 3.24. Values of δ are dissimilar by as much as 0.2 and as little as 0.01. Values of β are dissimilar by as much as 0.06 and as little as 0.001. Because of the large error bars in δ fit with transmission and because it is difficult to obtain accurate values for δ with transmission data, we refit our transmission data, fixing δ to be those values we obtained by fitting reflection data. As can be seen from Figure 3.25, β values

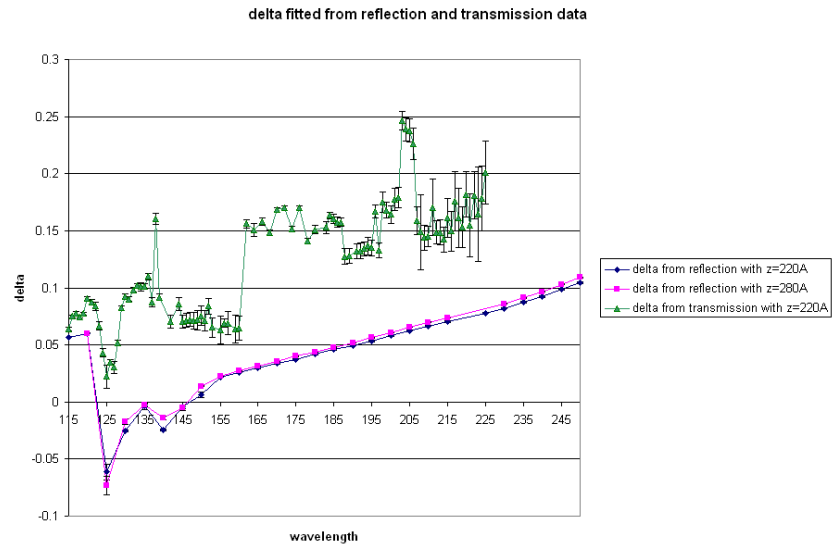


Figure 3.23: A comparison of δ values obtained by fitting reflection data and values obtained by fitting transmission data.

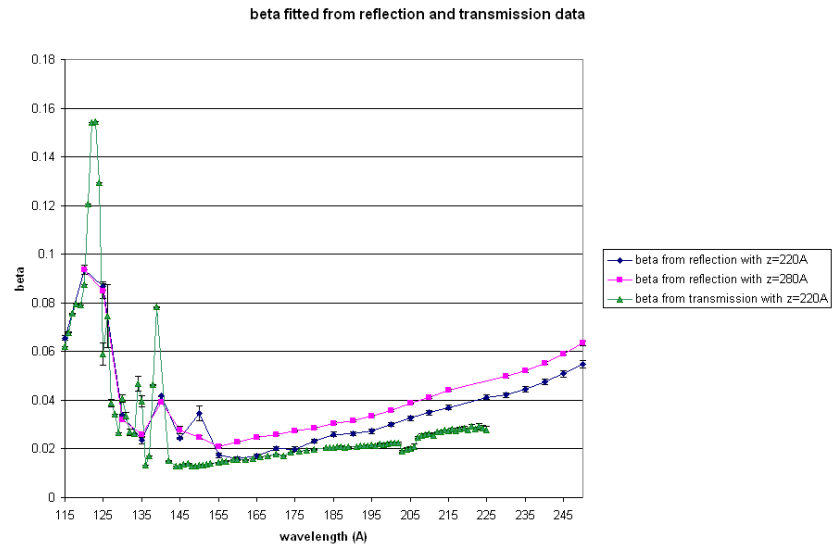


Figure 3.24: A comparison of β values obtained by fitting reflection data and values obtained by fitting transmission data.

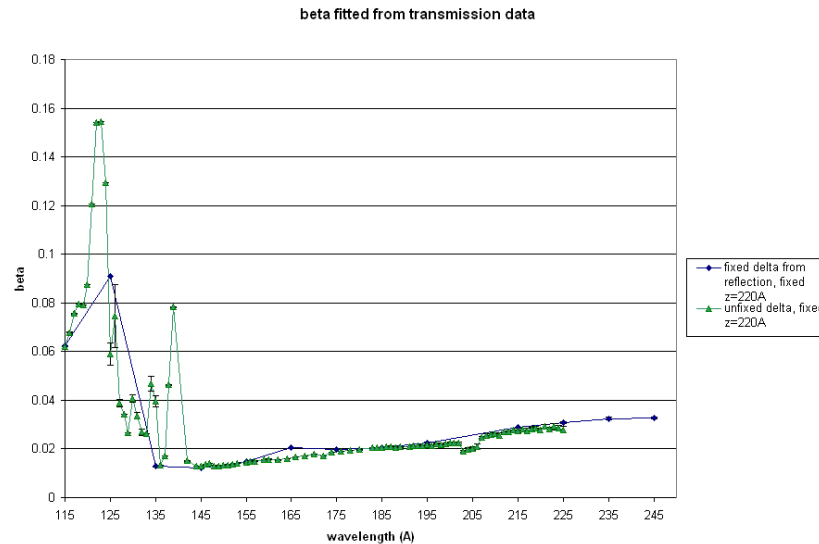


Figure 3.25: A comparison of β values obtained by fitting transmission data with an unfixed δ and then with a fixed δ obtained by fitting reflectance data.

did not change significantly when we used fixed values for δ obtained from the fits of reflection data. This is significant because it tells us that δ values obtained from reflection data fits are not only independent of film thickness in reflection data, they are independent of β values in transmission data. This makes us very confident in the accuracy of the δ values obtained from reflection data fits.

However, since the β values did not change in the transmission data when we changed the δ values, we still have two sets of values for β , one obtained with reflection and one with transmission measurements (see Figure 3.22). The value of β also depends on the thickness of the film, which we don't know. We tried refitting our reflectance data with fixed values of β obtained from fitting transmittance data, but the fits were significantly worse. In most cases, an error bar on β of 0.02 would not make significant errors in predicting the reflectance of a multilayer. However, for

thorium oxide we have found that δ and β are very similar in value. Reflectance of a boundary at normal incidence is given approximately by the equation

$$R \approx \frac{\delta^2 + \beta^2}{4} \quad (3.2)$$

If, for example, at a wavelength of 210 Å we have found δ to be 0.068. Transmittance fits give a β value of 0.026 while reflectance fits with a film thickness of 220 Å give a β value of 0.035. Thus β fitted with transmittance gives a reflectance at normal incidence of approximately 0.13% while β fitted with reflectance gives a value of 0.15%.

Chapter 4

Conclusions

We have characterized the roughness of our sample and have attempted to account for this roughness using three methods. We have found that: thorium has a naturally rough surface. Over a 100x100 nm area, RMS roughness is 3.6 nm. Over a 1000x1000 nm area, RMS roughness is 4.3 nm. In our sample, oxygen has interdiffused nearly linearly for 50 Å. The Debye-Waller factor corrects our data well for low angles. The Nevot-Croce factor corrects our data well for low and high angles. The finite differences approximation corrects our data very well for low and middle angles. We conclude that the best way to account for roughness in our program is to employ a combination of the Nevot-Croce factor and the finite distances approximation.

We have found values for δ for thorium oxide in the region from 115 – 250 Å. We have found that we cannot find β values that we believe in this region because reflectance and transmittance measurements give us two different and irreconcilable sets of data. We are unsure at this point why the two measurements give us different answers. We hope that future research (depositing on photodiodes) will help resolve this issue. We believe our values for δ despite this problem because they are relatively independent of thickness in reflection data and relatively independent of β in

transmission data. Since δ and β are so close together in this region, our value for β makes a significant difference in predicting how thorium oxide will reflect. For this reason we will continue to research this material.

Bibliography

- [1] Jedediah Edward Jensen Johnson, *Thorium-based Mirrors for High Reflectivity in the EUV*, Brigham Young University, Provo UT, 2004.
- [2] <http://www-cxro.lbl.gov/>
- [3] David J. Griffiths, *Introduction to Electrodynamics, Third Edition*, Prentice Hall, Upper Saddle River, NJ, 1999.
- [4] Eberhard Spiller, *Soft X-ray Optics*, SPIE Optical Engineering Press, Bellingham, WA, 1994.
- [5] L. G. Parratt, Phys. Rev. **95**, 2 (1954).
- [6] V. G. Kohn, Phys. Stat. Sol. (b) **187**, 61 (1995).
- [7] F. James, *MINUIT, Function Minimization and Error Analysis*, CERN Program Library, Geneva, Switzerland, 1998.
- [8] V. Holy, J. Kubena, and I. Ohlidal, Phys. Rev. B **47**, 23 (1993).
- [9] L. Nevot, B. Pardo, and J. Corno, Revue Phys. Appl. **23**, (1988).
- [10] P. Debye, Verh. D. Deutsch. Phys. Ges. **15**, 22 (1913).
- [11] P. Croce and L. Nevot, J. De Physique Appliquee **11**, 5 (1976).

[12] <http://www.moxtek.com/>

[13] <http://www-als.lbl.gov/als/>